

Current-voltage curves and operational stability in hot-carrier solar cell

Cite as: J. Appl. Phys. 127, 183102 (2020); doi: 10.1063/5.0002934

Submitted: 29 January 2020 · Accepted: 28 April 2020 ·

Published Online: 14 May 2020



K. Kamide^{a)}

AFFILIATIONS

Renewable Energy Research Center, National Institute of Advanced Industrial Science and Technology (AIST), Koriyama, Fukushima 963-0298, Japan

^{a)}Author to whom correspondence should be addressed: kenji.kamide@aist.go.jp

ABSTRACT

Current-voltage (I-V) curves and operational stability of hot-carrier solar cells are studied by a non-equilibrium theory considering three characteristic timescales of the hot-carrier dynamics (timescales for the extraction, equilibration, and thermalization). We find a hysteresis behavior in the I-V curves of high-efficiency hot-carrier solar cells, which could result in an operational instability. For practical application, we point out two types of instabilities that can degrade the device efficiency: one is intrinsic in a single cell and the other arises when plural cells are series-connected. It is also found that particle-number non-conserving processes, Auger recombination and impact ionization, increase the stability, showing an advantage of using a semiconductor material with a large Auger recombination coefficient for the light absorber.

© 2020 Author(s). All article content, except where otherwise noted, is licensed under a Creative Commons Attribution (CC BY) license (<http://creativecommons.org/licenses/by/4.0/>). <https://doi.org/10.1063/5.0002934>

I. INTRODUCTION

The hot-carrier solar cell (HCSC)¹ is one of the third-generation photovoltaic cells to achieve a high power conversion efficiency largely exceeding the detailed-balance limit, known as the Shockley-Queisser (SQ) limit.² It can have high efficiency by extracting hot carriers, generated by 6000 K blackbody radiation from the Sun, before they cool down to the lattice temperature of the absorber (thermalization). Recently, some progresses are found in experimental reports on HCSCs. An unexpectedly slow carrier cooling in a few nanoseconds was observed in Perovskite solar cells.³ In addition, hot-carrier effects were observed in a quantum-well-based solar cell, thanks to the developments in characterization technologies.⁴

A main reason why HCSCs are attractive is the high conversion efficiency achievable with a single layer of the light absorber in ideal cases (66% and 85% under unconcentrated and full concentrated illumination, respectively, according to the original theory¹). Later, the theoretical efficiencies were reassessed based on a theoretical model for a real cell, treating non-ideal cases where thermalization of the hot carriers cannot be neglected by introducing a finite thermalization time τ_{th} (which is infinity in an ideal case¹). Takeda *et al.*^{5–7} showed that the

conversion efficiencies achievable with realistic settings are around 50% for $\tau_{th} = 1$ ns and an illumination of 1000 suns (a practical limit for a concentration factor). Although the efficiency of the real HCSCs can be reduced considerably from the ideal values,¹ the high efficiency, 50%, achievable with a single absorber is still attractive.

The past theoretical papers mainly focus the conversion efficiencies at the max power conditions, while the current-voltage (I-V) characteristics have been rarely discussed.^{5–8} The main reason might be related to an issue raised by Würfel *et al.*,⁹ where it is claimed that the particle-number conserving (PC) model¹ predicts less reliable I-V curves with unrealistically high hot-carrier temperatures. In the paper, it is also claimed that including particle-number non-conserving processes, e.g., impact ionization (II) and Auger recombination (AR), which naturally come into play at high carrier temperatures, is necessary to predict reliable I-V curves for HCSCs, which, however, is not an easy task in simulation. A theoretical paper including the effect of II and AR processes gave a hysteresis behavior in the I-V curves, implying a possible operational instability in the HCSCs.¹⁰ However, sufficient discussion on the reliable I-V curves under realistic conditions in relation to the operational stability is still lacking.

Here, we study the I–V curves and the conversion efficiency of HCSCs with a stability analysis performed at the same time, based on a nonequilibrium theory.^{6,11} In this model, we introduce three timescales for the carrier dynamics relevant to HCSCs: a carrier-extraction time τ_{out} , a carrier-equilibration time τ_{eq} , and a carrier-thermalization time τ_{th} . For more reliable I–V curves, we also consider the effects of II and AR processes by using an Auger coefficient, C_{AR} , as an established parameter for the strength. We show that a hysteresis behavior is found in the I–V curves and causes instability on the steady-state operation in one-cell device and/or in a module of series-connected plural HCSCs. Moreover, it is also found that II and AR effects can stabilize the steady states of HCSCs and a stable operation with a high conversion efficiency above 50% could be obtained with an absorber of $E_g = 0.93$ eV under an illumination of 1000 suns, if the absorber has a large AR coefficient, $C_{\text{AR}} \geq 10^{-28}$ cm⁶/s.

II. MODELING

In this paper, we perform a numerical simulation based on a theoretical model including the three timescales of the carrier dynamics, τ_{out} , τ_{eq} , and τ_{th} . To introduce these timescales, we show Fig. 1 describing the dynamics of photocarriers after they are generated in a semiconductor by a short pulse of light until they thermalize at the lattice temperature. The initial non-thermal (non-equilibrium) state, whose energy distribution function directly reflects an energy spectrum of the excitation light [Fig. 1(a)], experiences an equilibration process in a timescale τ_{eq} [Fig. 1(b)], followed by a thermalization process in a timescale τ_{th} [Fig. 1(c)]. As described in Sec. II A, τ_{eq} and τ_{th} are material- and carrier-density-dependent

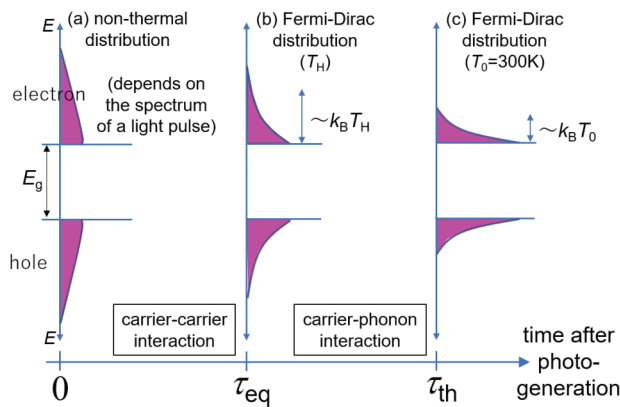


FIG. 1. Time evolution of the energy distribution function of the carriers in a semiconductor after they are generated by a short pulse of light (with a broad energy spectrum). The initial non-thermal distribution [(a)] evolves into a thermal one (Fermi-Dirac distribution) with a hot-carrier temperature T_H (higher than the lattice temperature T_0) in a time scale τ_{eq} [(b)], which is caused by an “equilibration,” i.e., the carrier–carrier interaction that preserves the total number and total energy of the carriers. The high-energy hot carriers lose the excess energy to form a Fermi-Dirac distribution with the lattice temperature T_0 in a longer time-scale, τ_{th} ($\gg \tau_{\text{eq}}$) [(c)], which is caused by a “thermalization,” i.e., the carrier–phonon interaction.

parameters of the absorber. A hot-carrier solar cell, which extracts the hot carriers (generated by a cw solar light) to the electrodes in a time scale τ_{out} , typically works in a regime of the parameter: $\tau_{\text{eq}} \ll \tau_{\text{out}} \ll \tau_{\text{th}}$.

There are several merits of using these timescales in the present study. First, these timescales can be deduced from time-resolved photoluminescence (PL) spectroscopy for τ_{th} ³ and τ_{eq} ^{12,13} and from time-of-flight charge collection¹⁴ for τ_{out} . Second, physical interpretation of the results for numerical simulations will become clearer by directly comparing the three timescales rather than by using a conductance as a parameter for the carrier transport.^{5–7} Moreover, in our previous modeling,¹¹ the carrier-extraction time τ_{out} is interpreted as a phenomenological parameter, which can incorporate a timescale spent for the carriers to travel through the absorber (by ballistic or diffusive transport), not only that spent at the contacts. In this sense, discussion using τ_{out} as a phenomenological parameter could give an insight also to Perovskite-based HCSCs,³ not only to those based on nanostructured inorganic semiconductors (like quantum wells and quantum dots).⁵

Let us start our modeling by defining these timescales and the practical ranges of the parameters.

A. Definitions of τ_{out} , τ_{eq} , and τ_{th} and the practical ranges

τ_{out} is introduced as a phenomenological parameter representing a characteristic time which charge-carriers spend after they are photogenerated inside the absorber until they are extracted to the contact electrodes.¹¹ In the rate equation, which will be given in Sec. II B, the energy distribution function in the absorber decays with a time constant τ_{out} . A HCSC uses energy-selective contacts as described in Sec. II B (Fig. 2). In a case where the carriers quickly travel through a thin absorber (of a thickness w) and their transport

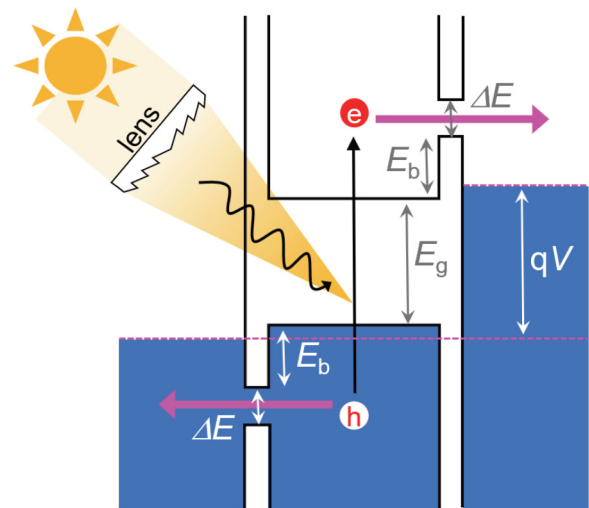


FIG. 2. Basic components and the energy diagram of a HCSC.

is limited almost at the contact by the weak link through energy-selective layers, τ_{out} is almost the same as the inverse of tunneling rate, $1/\gamma_{\text{esc}}$, determined at the contact. If a single quantum level (e.g., in a quantum dot) is used for the energy selection,⁵ $1/\gamma_{\text{esc}}$ can be estimated from the homogeneous linewidth at the peak in the current-voltage characteristics.¹⁵ Many experiments show the linewidth $\hbar\gamma_{\text{esc}}$ larger than a meV, meaning that $1/\gamma_{\text{esc}}$ is normally less than a picosecond ($=10^{-12}$ s). In the other case where their diffusive or ballistic transport inside the absorber takes a much longer time than that spent at the contact ($1/\gamma_{\text{esc}}$), their transport is limited by the finite carrier velocity v inside the absorber or a large thickness w . In the latter case, τ_{out} may be estimated roughly by w/v . Interpolating between the two cases, τ_{out} may be given by $\tau_{\text{out}} = 1/\gamma_{\text{esc}} + w/v$. It is known that a velocity of carriers inside semiconductors is bounded by the saturation velocity, i.e., the maximum velocity of carriers under a strong electric field, which is roughly 10^5 m/s.¹⁶ Thermal velocity of carriers at a temperature T , $v_T = \sqrt{3k_B T/m_c}$, is also of the same order as the saturation velocity for T between 300 K and 2000 K. By setting a maximum velocity, v_{max} , to 10^5 m/s, τ_{out} is bounded by its least value, w/v_{max} , which is 1 ps ($=10^{-12}$ s) for $w = 100$ nm and 10 ps ($=10^{-11}$ s) for $w = 1000$ nm = 1 μm . We adopted this rough estimation and performed simulations under $\tau_{\text{out}} \geq w/v_{\text{max}}$ considering the absorber of thickness $w \geq 100$ nm. Of course, this will give an optimistic result in the simulation of a hot-carrier solar cell that requires fast carrier extraction. In a case where their transport is diffusive (not ballistic), the travel time replaced by w^2/D (D is the diffusion coefficient) should be longer than w/v_{max} . For example, w^2/D is estimated to be 50 ps for GaAs ($D = 200$ cm²/s for electrons) of 1 μm thickness.

τ_{eq} , an equilibration time of the carriers, is introduced as a characteristic time that the photogenerated carriers inside the absorber spend until they share the kinetic energies as a result of many cycles of elastic collisions with each other, normally via the Coulomb interaction, and reach an equilibrium state characterized by a hot-carrier temperature, T_H [Fig. 1(b)]. T_H can differ from the Sun's radiation temperature ($T_{\text{sun}} = 6000$ K) and the ambient temperature ($T_0 = 300$ K). Frequent carrier-carrier scatterings mean a short τ_{eq} . A short τ_{eq} is an essential factor in hot-carrier solar cells, since the high-energy hot-carrier population cannot be built up without the efficient equilibration process. In addition, a fast equilibration before the extraction ($\tau_{\text{eq}} < \tau_{\text{out}}$) is required to avoid depletion of the carriers to be extracted by immediately filling the states in the extraction energy window prior to the next extraction (see Sec. 8.4.3 of Ref. 7). This latter condition is also essential to achieve a high efficiency. Ultrafast hot-carrier dynamics were intensively studied in semiconductors in late 1980's shortly after a development of pump and probe spectroscopy using femtosecond short-pulse lasers.¹⁷ It is well established that the rate for the carrier-carrier scattering $1/\tau_{\text{eq}}$ increases with the density of excited carriers.^{12,13} In Ref. 12, 13, τ_{eq} was reported to range between a subpicosecond and a picosecond for the carrier density between 10^{15} and 10^{17} cm⁻³ in a bulk GaAs sample. The carrier density is quite high, slightly below the degeneracy point known as the Mott density (above which an optical gain for lasing starts to appear¹⁸). However, a such high density can be reached in hot-carrier solar

cells, which are using an ultrathin absorber under highly concentrated illumination. Seeing the above, we present device simulation by setting $\tau_{\text{eq}} = 10^{-12}$ s. We confirmed that a simulation using the density-dependent τ_{eq} gave results similar to those obtained with $\tau_{\text{eq}} = 10^{-12}$ s (not shown).

τ_{th} , a carrier-thermalization time, is introduced as a characteristic time that is necessary for the hot carriers to lose its energy, by emitting lattice phonons in the absorber, and form a thermal equilibrium state with the ambient temperature T_0 [Fig. 1(b)]. Therefore, τ_{th} is shorter for a stronger carrier-phonon interaction and for a larger number of phonon modes relevant to the cooling process. A longer τ_{th} is required for HCSCs to have high efficiencies since the hot carriers must be extracted before their kinetic energies are lost as heat.¹ τ_{th} can be estimated theoretically by taking into account the phonon modes that dominate the carrier cooling processes¹¹ and directly measured in experiments. In many bulk semiconductors, τ_{th} is known to range in several picoseconds (see Refs. 19 and 20 for GaAs and Refs. 21, 22, and 23 for silicon). However, the thermalization time, τ_{th} , can be prolonged due to several mechanisms in a HCSC under a strong illumination. The most known is a phonon bottleneck effect occurring due to enhanced reabsorption of highly populated optical phonons at high carrier densities.^{20,24} Such an effect is enhanced further in nanostructured semiconductors such as quantum wells and quantum dots.²⁵⁻²⁷ In GaAs multiple quantum wells, τ_{th} is found to reach many hundreds of picoseconds at high intensity of light (corresponding to the carrier densities above 10^{18} cm⁻³).^{28,29} Recently, a similar slow carrier cooling at high intensity of light has been found in perovskite absorbers³ and reported in a number of papers (see Ref. 30 and references therein). In a perovskite solar cell, τ_{th} can exceed a few nanoseconds.³ By seeing these reports, we set $\tau_{\text{th}} = 10^{-9}$ s (1 ns) in this paper.

B. A rate equation model

A HCSC in the present study is described by the energy diagram shown in Fig. 2. It consists of an absorber with a bandgap E_g , two energy-selective contacts, and two electrodes for extracting electrons and holes separately as its basic components. The energy-selective contacts are described by an energy level at the lower edge and a bandwidth of the passband, i.e., E_b and ΔE in Fig. 2. This bandpass energy-selective contacts could be implemented with resonant-tunneling structures.⁵ The HCSC is illuminated with highly concentrated solar light whose concentration factor CR is set at 1000 in the simulation as a practical limit.^{5-7,31}

In addition to the above setup, we also assume an ideal situation which can be realized in principle and also assumed previously in the similar studies.^{6,8,11} We assume perfect absorption for photons with an energy above the absorption edge, i.e., a step function-like absorptivity, $\theta(E - E_g)$. To implement this with a 100-nm-thick absorber, an efficient light trapping is necessary. A homogeneous carrier distribution is assumed in the absorber, which is a reasonable assumption for $w \ll L_D$ ($=$ a diffusion length of the carriers). A radiative limit with neglecting nonradiative recombination of the carriers is taken, where perfect passivation of the absorber's surface is implicitly assumed so that the surface recombination is also negligible. A perfect carrier selectivity is

assumed for the contacts, i.e., only the conduction electrons are assumed to be extracted to the electron contact, and only the valence holes are assumed to be extracted to the hole contact. An absorber is made of a direct-gap semiconductor for which the carriers are described by an effective two-band model with an equivalent effective mass $m_c = 0.1m_0$ (m_0 is the rest mass of an electron), both for conduction electrons and valence holes. In addition, lattice temperatures in the whole system (absorber, contacts, and energy-selective layers) are set at a room temperature T_0 ($=300$ K). These simplifications are just for the sake of clarity in comparing with results of a previous study.⁶ The Sun's spectrum is approximated by the 6000 K blackbody radiation, and the light intensity is normalized to 1 kW/m^2 at a concentration factor of unity. The author believes that this simple modeling will not change the main conclusion largely even if other realistic factors were also considered.

Following the formulation in the previous papers,^{6,11} we can derive a rate equation for the distribution function of the carriers in the absorber, n_E , an average population in microscopic states at an energy, $E > 0$ (E is measured from the band edges). Since we adopt an electron-hole symmetric model with an equivalent effective mass $m_c (=m_e=m_h=0.1m_0)$, the energy distribution functions for conduction electrons and valence holes are equivalent as well. The microscopic rate equation to be solved is

$$\frac{d}{dt}n_E = \mathcal{R}_E^{\text{sun}} - \mathcal{R}_E^{\text{rad}} - \mathcal{R}_E^{\text{out}} - \mathcal{R}_E^{\text{eq}} - \mathcal{R}_E^{\text{th}} = 0, \quad (1)$$

where $\mathcal{R}_E^{\text{sun}}$ represents the generation rate by the light absorption, $\mathcal{R}_E^{\text{rad}}$ is the loss rate by the radiative recombination, $\mathcal{R}_E^{\text{out}}$ represents the loss rate due to the carrier extraction to the contact, $\mathcal{R}_E^{\text{eq}}$ represents the equilibration rate toward an equilibrium among the carriers inside the absorber, and $\mathcal{R}_E^{\text{th}}$ represents the thermalization rate toward a thermal equilibrium at the lattice temperature (an equilibrium between carriers and lattice phonons). The last equation in Eq. (1) is satisfied in the steady state. The terms in the rate equation are, respectively, given by¹¹

$$\mathcal{R}_E^{\text{sun}} = \frac{2j_{\text{sun}}(E_g + 2E)}{qw\mathcal{D}_e(E)}, \quad (2)$$

$$\mathcal{R}_E^{\text{rad}} = \frac{c}{\pi^2 w} \left(\frac{1}{\hbar c} \right)^3 \times \frac{(E_g + 2E)^2}{\mathcal{D}_e(E)} \times \frac{n_E^2}{1 - 2n_E}, \quad (3)$$

$$\mathcal{R}_E^{\text{out}} = \frac{\mathcal{F}_{E_b, \Delta E}(E)}{\tau_{\text{out}}} (n_E - f_{\mu_{\text{out}}, T_0}(E)), \quad (4)$$

$$\mathcal{R}_E^{\text{eq}} = \frac{1}{\tau_{\text{eq}}} (n_E - f_{\mu_H, T_H}(E)), \quad (5)$$

$$\mathcal{R}_E^{\text{th}} = \frac{1}{\tau_{\text{th}}} (n_E - f_{\mu_{\text{th}}, T_0}(E)), \quad (6)$$

where $\mathcal{D}_e(E) = d_e \sqrt{E}$ with $d_e \equiv (2m_c)^{3/2}/(2\pi^2 \hbar^3)$ is the density of states per unit volume per unit energy at an energy E for

conduction electrons in the absorber and $j_{\text{sun}}(E) \equiv CR \times \mathcal{N} \times E^2 \times (\exp[E/(k_B T_{\text{sun}})] - 1)^{-1}$ is the photogenerated charge-current density in the absorber per unit area per unit energy, which are defined with a concentration factor CR , the radiation temperature of the Sun $T_{\text{sun}} (=6000 \text{ K})$, and a normalization factor \mathcal{N} ($\equiv 2155 \text{ W m}^{-2} \text{ eV}^{-4}$) introduced to normalize the power density of the illumination as $\int_0^\infty E \times j_{\text{sun}}(E) dE = 1000 \text{ W/m}^2$ at $CR = 1$. q is the elementary charge, c is the speed of light in a vacuum, $\hbar (= \hbar/(2\pi))$ is the Planck constant, and k_B is the Boltzmann constant. The effect of energy-selective contacts is taken into account through a window function, $\mathcal{F}_{E_b, \Delta E}(E)$ in Eq. (4), which is unity for $E_b \leq E \leq E_b + \Delta E$ and otherwise zero (Fig. 2). A different function for the transmission window was used previously (e.g., a Gaussian function in Ref. 6). However, we consider that the difference will not cause a large difference in the final result. In the rate equation in Eq. (1), three terms, $\mathcal{R}_E^{\text{out}}$, $\mathcal{R}_E^{\text{eq}}$, and $\mathcal{R}_E^{\text{th}}$, will relax the carrier distribution function n_E toward different thermal equilibrium distribution functions, defined by the Fermi-Dirac function $f_{\mu, T}(E) \equiv (e^{(E-\mu)/(k_B T)} + 1)^{-1}$, with different temperatures and chemical potentials with different relaxation time constants, τ_{out} , τ_{eq} , and τ_{th} . Since the first term $\mathcal{R}_E^{\text{out}}$ represents the carrier extraction to the contact, the temperature T_0 and the chemical potential μ_{out} in $f_{\mu_{\text{out}}, T_0}(E)$ are those given in the contacts and its chemical potential is directly related to an output voltage V of the hot-carrier solar cell, as given by $\mu_{\text{out}} = (qV - E_g)/2$. Therefore, μ_{out} is an input parameter in the simulation. On the other hand, at this moment, μ_H , T_H , and μ_{th} are yet-unknown auxiliary parameters, which will be determined later in a manner that was introduced in Ref. 6.

Let us solve at first Eq. (1) under the steady-state condition while leaving these parameters (μ_H , T_H , and μ_{th}) to be determined later. In the steady state, Eq. (1) can be viewed as a quadratic equation in terms of the variable n_E [this can be checked by multiplying $1 - 2n_E$ on the both sides of Eq. (1)]. Therefore, two exact solutions can be found: one solution will describe a solar cell operation with $n_E < 1/2$ (by which the absorber works as a light absorber) and the other solution will describe a laser operation with $n_E > 1/2$ (by which the absorber works as a light emitter with a population inversion, i.e., an optical gain required for lasers). We choose the former solution appropriate for a solar cell, which is explicitly given by

$$n_E = \frac{B - \sqrt{B^2 - 4AC}}{2A} = \frac{a + 2b + 2g - \sqrt{(a - 2b - 2g)^2 + 4(b + g)r}}{4a - 2r}, \quad (7)$$

where $A = 2a - r$, $B = a + 2b + 2g$, and $C = b + g$ with

$$a = \frac{\mathcal{F}_{E_b, \Delta E}(E)}{\tau_{\text{out}}} + \frac{1}{\tau_{\text{eq}}} + \frac{1}{\tau_{\text{th}}} > 0, \quad (8)$$

$$b = \frac{\mathcal{F}_{E_b, \Delta E}(E)f_{\mu_{\text{out}}, T_0}(E)}{\tau_{\text{out}}} + \frac{f_{\mu_H, T_H}(E)}{\tau_{\text{eq}}} + \frac{f_{\mu_{\text{th}}, T_0}(E)}{\tau_{\text{th}}} > 0, \quad (9)$$

$$g = \mathcal{R}_E^{\text{sun}} = \frac{2j_{\text{sun}}(E_g + 2E)}{qw\mathcal{D}_e(E)} > 0, \quad (10)$$

$$r = \frac{c}{\pi^2 w} \left(\frac{1}{\hbar c} \right)^3 \frac{(E_g + 2E)^2}{\mathcal{D}_e(E)} > 0. \quad (11)$$

In this way, the variable n_E can be determined exactly, whereas the three auxiliary parameters μ_H , T_H , and μ_{th} are yet to be determined. It should be remarked that, in the limit of $\tau_{eq} \rightarrow +0$, the exact solution in Eq. (7) safely reproduces a thermal equilibrium distribution function at a hot-carrier temperature, $n_E = f_{\mu_H, T_H}(E)$ [for $f_{\mu_H, T_H}(E) < 1/2$], which was assumed in the previous study.⁵

The simple exact solution given above was obtained, thanks to a simplification in the modeling mentioned at the beginning of this subsection. By restricting the material of the absorber to a direct-gap semiconductor, distribution functions at different energy levels, n_E and $n_{E'}$ with $E \neq E'$, are decoupled in the equation. Even when effective masses of electrons and holes are different, distribution functions for electrons, n_E^e , and for holes, $n_{E'=m_e/m_h E'}^h$ are exclusively coupled in the rate equation¹¹ and, therefore, an exact solution can be found in a similar manner. However, the solution will become more complicated than that obtained under the electron-hole symmetry. If the same formulation was applied to, e.g., an absorber of indirect-gap semiconductor,¹¹ distribution functions at different energy levels are coupled in the rate equation (since the radiative recombination term, $\mathcal{R}_E^{\text{rad}}$, is given by an integration $\propto \int M_{E,E'} n_E^e n_{E'}^h dE'$) and only the numerical solution will be available. Normally, we can disregard the latter case of an indirect-gap semiconductor especially for a HCSC, since a HCSC requires a strong light absorber for which a direct-gap semiconductor is normally selected. Moreover, we should also notice that a similar complication occurs even for a direct-gap semiconductor if three hole bands (heavy-, light-, and split-hole bands) are included in the model.

Furthermore, it should be mentioned that the simple expressions for the relaxation terms, $\mathcal{R}_E^{\text{eq}}$ and $\mathcal{R}_E^{\text{th}}$ given in Eqs. (5) and (6), introduced based on the relaxation time approximation also have a great impact in finding the exact solution in Eq. (7). We consider the relaxation time approximation works well if values for yet-undetermined parameters, μ_H , T_H , and μ_{th} , are determined appropriately, as presented below.

Finally, the three unknown parameters, μ_H , T_H , and μ_{th} are now determined by a procedure given in Ref. 6. As mentioned in Subsection II A, the carrier-equilibration process described by the equilibration rate $\mathcal{R}_E^{\text{eq}}$ in Eq. (1) originates from the elastic carrier-carrier scattering via the Coulomb interaction. Except for number-nonconserving impact ionization and Auger recombination processes, which will be discussed separately in Sec. III B, the equilibration process does not change both the total number and total energy of the hot carriers. These conditions are incorporated in the theory by assigning following constraints:

$$\int \mathcal{D}_e(E) \mathcal{R}_E^{\text{eq}} dE = \int \mathcal{D}_e(E) \frac{n_E - f_{\mu_H, T_H}(E)}{\tau_{eq}} dE = 0, \quad (12)$$

$$\int E \mathcal{D}_e(E) \mathcal{R}_E^{\text{eq}} dE = \int E \mathcal{D}_e(E) \frac{n_E - f_{\mu_H, T_H}(E)}{\tau_{eq}} dE = 0, \quad (13)$$

where Eqs. (12) and (13) correspond to conservation of the total number and total energy of the hot carriers, respectively. Similarly, the carrier cooling process described by the thermalization rate $\mathcal{R}_E^{\text{th}}$ in Eq. (1) originates from carrier-phonon scattering. Obviously, the number of carriers is conserved during this process, while excess energies of hot carriers are dissipated into the lattice phonons. The carrier number conservation in this thermalization process can be incorporated by an additional constraint,

$$\int \mathcal{D}_e(E) \mathcal{R}_E^{\text{th}} dE = \int \mathcal{D}_e(E) \frac{n_E - f_{\mu_{th}, T_0}(E)}{\tau_{th}} dE = 0. \quad (14)$$

Since n_E is already found in Eq. (7) as a function of the unknown parameters (μ_H , T_H , and μ_{th}), these three constraints, Eqs. (12)–(14), can be viewed as coupled equations to determine them. Since they are coupled nonlinear equations, the solutions can be found only numerically except for certain limiting cases.

In this way, the carrier distribution function in the absorber is fully determined by the simulation. Using the carrier distribution function with μ_H , T_H , and μ_{th} , we can evaluate the output charge-current density, I , per unit area^{6,11} as a function of an output voltage V by

$$I = qw \int_0^\infty \mathcal{D}_e(E) \mathcal{R}_E^{\text{out}} dE \equiv I_{\text{out}} \quad (15)$$

or by

$$I = qw \int_0^\infty \mathcal{D}_e(E) (\mathcal{R}_E^{\text{sun}} - \mathcal{R}_E^{\text{rad}}) dE \equiv I_{\text{sun}} - I_{\text{rad}}, \quad (16)$$

where I_{sun} and I_{rad} represent the current densities due to the photo-generation and the radiative recombination loss, respectively. Then, a power conversion efficiency η (%) of this hot-carrier solar cell is evaluated as usual by

$$\eta \equiv 100 \times IV / (CR \times 1000 \text{ W/m}^2). \quad (17)$$

Finally, we would like to mention the numerics in the device simulation shown below. Equations (12)–(14) are solved by limiting the integration range to $0 < E \leq 6 \text{ eV}$, assuming a high-energy cutoff of 6 eV. This cutoff energy was chosen to be large enough to cover a whole range of the Sun's spectrum to be absorbed (except below the bandgap energy). Then, we discretized the energy domain, $0 < E \leq 6 \text{ eV}$, with a finite mesh size $dE = 5 \text{ meV}$. This mesh size was chosen so that $dE < k_B T_0 = 26 \text{ meV}$, which ensures that dE is much smaller than the thermal energy of the hot carriers $\sim k_B T_H$.

C. Stability analysis on multiple steady states

The rate equation model presented in Subsection II B is mathematically classified as a nonlinear problem [a quadratic equation, Eq. (1) with three constraints, Eqs. (12)–(14)]. As seen in Subsection II B, we have chosen one branch from the two exact

solutions to the quadratic equation (corresponding to $n_E < 1/2$). However, even for this case, multiple steady-state solutions with different values of the auxiliary variables (T_H, μ_H, μ_{th}), may exist. As found below, we find in some cases three steady-state solutions for a set of parameters. Therefore, it is necessary to discriminate the multiple solutions to tell which solutions will correctly describe the real operation of a HCSC. In this paper, we study Lyapunov stability³² of the steady states to address this issue in the numerical simulation. Here, we briefly summarize the method of this stability analysis.

In the stability analysis, we will check the dynamical stability of the hot carriers, whose instability can be triggered by a small fluctuation around the steady state [n_E given in Eq. (7)]. The small fluctuation in the carrier distribution function, $n_E \rightarrow n_E + \delta n_E$, will cause small fluctuations in the auxiliary variables, $T_H \rightarrow T_H + \delta T_H$, $\mu_H \rightarrow \mu_H + \delta \mu_H$, and $\mu_{th} \rightarrow \mu_{th} + \delta \mu_{th}$, since they are related by the strict constraints, Eqs. (12)–(14). First, by inserting them into Eq. (1) and expanding the equation to the first order in the small fluctuations ($\mathcal{O}(\delta)$), we have an equation of motion for δn_E ,

$$\begin{aligned} \frac{d}{dt} \delta n_E = & - \left(2r \frac{n_E(1-n_E)}{(1-2n_E)^2} + a \right) \delta n_E + \frac{1}{\tau_{eq}} \frac{\partial f_{\mu_H, T_H}}{\partial \mu_H} \delta \mu_H \\ & + \frac{1}{\tau_{eq}} \frac{\partial f_{\mu_H, T_H}}{\partial T_H} \delta T_H + \frac{1}{\tau_{th}} \frac{\partial f_{\mu_{th}, T_0}}{\partial \mu_{th}} \delta \mu_{th}. \end{aligned} \quad (18)$$

In a similar manner, we expand the three constraints, Eqs. (12)–(14) to the first order in the small fluctuations, by which we find

$$\begin{pmatrix} \delta N \\ \delta U \end{pmatrix} = \hat{A} \begin{pmatrix} \delta \mu_H \\ \delta T_H \end{pmatrix}, \quad \hat{A} \equiv \begin{pmatrix} A_{11} & A_{12} \\ A_{21} & A_{22} \end{pmatrix} \quad (19)$$

from Eqs. (12) and (13) and

$$\delta N = B_{11} \delta \mu_{th} \quad (20)$$

from Eq. (14). Here, δN and δU defined by

$$\delta N \equiv \int \mathcal{D}_e(E) \delta n_E dE, \quad (21)$$

$$\delta U \equiv \int \mathcal{D}_e(E) E \delta n_E dE, \quad (22)$$

represent fluctuations in the total number and energy densities, respectively. The matrix elements of \hat{A} and B_{11} are given by

$$\begin{aligned} A_{11} & \equiv \int \mathcal{D}_e(E) \frac{\partial f_{\mu_H, T_H}}{\partial \mu_H} dE \\ & = \frac{1}{k_B T_H} \int \mathcal{D}_e(E) f_{\mu_H, T_H} (1 - f_{\mu_H, T_H}) dE, \end{aligned} \quad (23)$$

$$\begin{aligned} A_{12} & \equiv \int \mathcal{D}_e(E) \frac{\partial f_{\mu_H, T_H}}{\partial T_H} dE \\ & = \frac{1}{k_B T_H^2} \int \mathcal{D}_e(E) (E - \mu_H) f_{\mu_H, T_H} (1 - f_{\mu_H, T_H}) dE, \end{aligned} \quad (24)$$

$$\begin{aligned} A_{21} & \equiv \int \mathcal{D}_e(E) E \frac{\partial f_{\mu_H, T_H}}{\partial \mu_H} dE \\ & = \frac{1}{k_B T_H} \int \mathcal{D}_e(E) E f_{\mu_H, T_H} (1 - f_{\mu_H, T_H}) dE, \end{aligned} \quad (25)$$

$$\begin{aligned} A_{22} & \equiv \int \mathcal{D}_e(E) E \frac{\partial f_{\mu_H, T_H}}{\partial T_H} dE \\ & = \frac{1}{k_B T_H^2} \int \mathcal{D}_e(E) E (E - \mu_H) f_{\mu_H, T_H} (1 - f_{\mu_H, T_H}) dE, \end{aligned} \quad (26)$$

$$\begin{aligned} B_{11} & \equiv \int \mathcal{D}_e(E) \frac{\partial f_{\mu_{th}, T_0}}{\partial \mu_{th}} dE \\ & = \frac{1}{k_B T_0} \int \mathcal{D}_e(E) f_{\mu_{th}, T_0} (1 - f_{\mu_{th}, T_0}) dE, \end{aligned} \quad (27)$$

where we have used properties of the Fermi–Dirac function

$$\begin{aligned} \frac{\partial f_{\mu, T}}{\partial \mu} & = \frac{1}{k_B T} f_{\mu, T} (1 - f_{\mu, T}), \\ \frac{\partial f_{\mu, T}}{\partial T} & = \frac{(E - \mu)}{k_B T^2} f_{\mu, T} (1 - f_{\mu, T}) \end{aligned}$$

in the second equation in Eqs. (23)–(27). Finally, by expressing $\delta \mu_H$, δT_H , and $\delta \mu_{th}$ in terms of δN and δU using Eqs. (19) and (20), we can now rewrite the equation of motion, Eq. (18), in a closed form of δn_E as

$$\frac{d}{dt} \delta n_E = \int \Lambda(E, E') \delta n_{E'} dE', \quad (28)$$

where the function $\Lambda(E, E')$ is found to be

$$\begin{aligned} \Lambda(E, E') = & - \left(2r(E) \frac{n_E(1-n_E)}{(1-2n_E)^2} + a(E) \right) \delta(E - E') \\ & + \frac{\frac{A_{22}}{k_B T_H} - \frac{E - \mu_H}{k_B T_H^2} A_{21}}{\det \hat{A}} \times \frac{f_{\mu_H, T_H}(E) (1 - f_{\mu_H, T_H}(E))}{\tau_{eq}} \mathcal{D}_e(E') \\ & + \frac{\frac{E - \mu_H}{k_B T_H} A_{11} - \frac{A_{12}}{k_B T_H}}{\det \hat{A}} \times \frac{f_{\mu_H, T_H}(E) (1 - f_{\mu_H, T_H}(E))}{\tau_{eq}} \mathcal{D}_e(E') E' \\ & + \frac{1}{k_B T_0 B_{11}} \times \frac{f_{\mu_{th}, T_0}(E) (1 - f_{\mu_{th}, T_0}(E))}{\tau_{th}} \mathcal{D}_e(E'). \end{aligned} \quad (29)$$

where $\delta(E - E')$ is the Dirac delta function having a pole at $E = E'$. In Eq. (29), the dependency on E and E' is shown explicitly.

As noted in Subsection II B, we have introduced a high-energy cutoff ($=6$ eV) and discretized the energy domain $0 < E \leq 6$ eV with a finite mesh size dE ($=5$ meV) in the numerical simulation for finding the steady-state solutions. We also use the same cutoff energy and the same mesh size in this stability analysis. Therefore, Eq. (28) are discretized in the same manner. The discretized version of the equation

$$\frac{d}{dt} \delta n_E = \sum_{E'} L_{E,E'} \delta n_{E'} \quad (30)$$

is a linear equation whose dynamics is described by matrix \hat{L} with a dimension 1200×1200 ($1200 = 6 \text{ eV} / 5 \text{ meV}$) whose matrix elements are given by

$$L_{E,E'} = \int_{E'-dE/2}^{E'+dE/2} \Lambda(E, E'') dE''. \quad (31)$$

Notice that matrix \hat{L} is a function of the steady state.

We determine the stability of the multiple steady-state solutions based on the eigenvalues of \hat{L} .³² If all the eigenvalues of \hat{L} have a negative real part, any small fluctuations will decay in time. In this case, we regard the steady-state solution to be Lyapunov stable. On the other hand, if \hat{L} have at least one eigenvalue with a positive real part, we regard the steady state to be Lyapunov unstable since the corresponding small fluctuation will grow exponentially in time and eventually cause an instability to the steady state.

III. RESULTS AND DISCUSSION

In this section, we show results of numerical simulation based on the rate equation model described in Sec. II with the I-V characteristics and stability being focused. In the simulation, we fixed following parameters: a bandgap of the absorber $E_g = 0.93$ eV, a concentration ratio $CR = 1000$, a thickness of the absorber $w = 100$ nm, a bandwidth of the energy-selective contacts $\Delta E = 0.1$ eV, a carrier-thermalization time $\tau_{th} = 1$ ns, and a carrier-equilibration time $\tau_{eq} = 1$ ps. These are the optimal values giving the maximum efficiency around 50% in Refs. 5 and 6, and the values for τ_{th} and τ_{eq} are shown to be feasible in Sec. II A.

In Sec. III A, a numerical simulation is performed with a particle-number conserving (PC) model where the number non-conserving processes (e.g., AR and II) are neglected. The output voltage, V , the lower edge of the passband of the energy-selective contacts, E_b (Fig. 2), and the carrier-extraction time τ_{out} are the input parameters in the simulation. In Sec. III B, the effect of AR and II is considered in the simulation by taking an Auger coefficient C_{AR} as a parameter indicating the strength. Therefore, V , E_b , τ_{out} , and C_{AR} are the input parameters in the simulation.

We would like to remind the reader that the illumination condition with a 6000-K blackbody spectrum is different from AM1.5D illumination used in Refs. 5 and 6, which will make a slight difference in the maximum efficiency and the optimal

parameters. In addition, the introduction of AR and II can shift the optimal parameters as well, while the change will not be large and our main conclusion in the present study will remain unchanged.

A. Main results: I-V curves and conversion efficiencies under the stable operation

Figure 3 shows the maximum conversion efficiency η_{max} plotted as a function of the carrier-extraction time τ_{out} , whereas the each point is obtained by optimizing V and E_b . Although the details will be explained later, the conversion efficiency η_{max} (squares, dashed, described as “upper branch”) is maximized to 53.1% at $\tau_{out} = 10^{-11}$ s. We notice that this optimal value fulfills a standard condition appropriate for HCSCs (mentioned at the beginning of Sec. II), $\tau_{eq} (=1 \text{ ps}) \ll \tau_{out} \ll \tau_{th} (=1 \text{ ns})$, implying that the framework of our simulation works well. In the following, we will discuss the I-V curves by setting τ_{out} at the optimal value 10^{-11} s.

Figure 4 shows the I-V curves obtained for different values of E_b . For $E_b = 0.23$ eV [Fig. 4(a)], we found the I-V curve continuously connects between the short-circuit and the open-circuit conditions ($V = 0$ and $I = 0$, respectively). The max conversion efficiency η_{max} is 46.5% (filled circle) and the fill factor is very high as 0.96. The open-circuit voltage, $V_{oc} = 1.055$ V exceeding $E_g/q = 0.93$ V is thanks to the energy barrier ($E_b > 0$) of the energy-selective contacts, which is a characteristic of a HCSC. The linear stability analysis (Lyapunov stability analysis) shows that all the points in the I-V curve are Lyapunov stable.

As E_b increases [Figs. 4(b)–4(c)], the I-V curve near the open-circuit condition $V \sim V_{oc}$ bends downward while the curve at the short-circuit side $I \sim I_{sun}$ remains unchanged. However, the I-V curve is continuous in the entire region between the open-circuit and short-circuit conditions for $0.24 \text{ eV} \leq E_b \leq 0.33 \text{ eV}$. As a result, there emerges a region of V with three values of I for a given voltage:

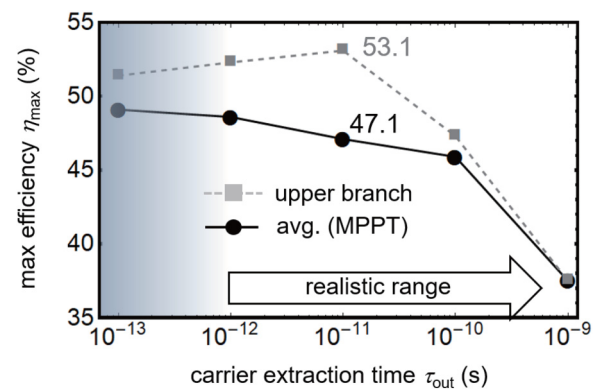


FIG. 3. The max conversion efficiency η_{max} of a HCSC determined as a function of carrier-extraction time, τ_{out} , by optimizing V and E_b (we set $E_g = 0.93$ eV, $CR = 1000$, $w = 100$ nm, $\Delta E = 0.1$ eV, $\tau_{th} = 1$ ns, and $\tau_{eq} = 1$ ps). The values are obtained at the max power point (MPP) in the upper branch of the I-V curves (gray, square, dashed) and also by a long-time average with a MPP tracking (black, filled circle, solid). The former is larger but unstable in a real operation, while the latter lower values will give a more reasonable estimation in real application (see the text explanation for details).

[$1.048 \text{ V} \leq V \leq 1.054 \text{ V}$ in Fig. 4(b) and $1.035 \text{ V} \leq V \leq 1.135 \text{ V}$ in Fig. 4(c)]. According to the linear stability analysis, the upper and lower branches of the I-V curve (black solid) are found to be stable, whereas the middle branch (red dashed) is found to be unstable. It should be noted that the latter unstable branch has a negative differential resistance while the other stable branches have normal positive differential resistances. As indicated by open circles on I-V curves in Figs. 4(b)–4(c), the max power points (MPPs) in the upper and lower branches are located at their end points where they meet with the middle unstable branch. Therefore, the MPPs are Lyapunov unstable in a strict sense and thus indicated by open circles in contrast to the stable MPP, a filled circle in Fig. 4(a).

For the larger E_b , the lower stable branch bends downward more strongly and disconnects completely from the middle

unstable branch as shown in Fig. 4(d). As a result, there emerge two stable I-V curves: the upper curve that ends at a large value of V corresponding to an unstable MPP [$\eta_{\max} = 52.5\%$ in Fig. 4(d)] and the lower curve with a stable MPP [$\eta_{\max} = 38.2\%$ in Fig. 4(d)]. The similar I-V curves are obtained for $0.34 \text{ eV} \leq E_b \leq 0.39 \text{ eV}$. As E_b becomes larger, the gap between the upper stable and middle unstable branches decreases, and the two branches merge at $E_b = 0.40 \text{ eV}$. For $E_b \geq 0.40 \text{ eV}$, they disappear simultaneously while the lower branch only remains as shown in Fig. 4(e). For this case, the short-circuit current is largely reduced from I_{sun} and the η_{\max} decreases significantly.

The above result is summarized in Fig. 5 where the max conversion efficiency η_{\max} is shown as a function of E_b separately for the upper and lower branches (blue circles and red squares, respectively). We should notice that although a large value of η_{\max} above 50% is found, the MPP is unstable in the upper branch in a strict sense. In Fig. 5, η_{\max} in the upper branch corresponds to the unstable MPP for $0.25 \text{ eV} \leq E_b \leq 0.39 \text{ eV}$, and the same is true in the lower branch for $0.25 \text{ eV} \leq E_b \leq 0.33 \text{ eV}$. These results imply that the η_{\max} must be considered carefully if it is located at the unstable MPP, whose operation could become unstable in real application.

Finally, we would like to mention two examples of instability in the device operation expected in real systems, which could reduce the device efficiency, in relation to those discussed above. The first example of the instabilities occurs when operating a single HCSC with a max power point tracking (MPPT) system. In practical application where the illumination condition can change with the weather, the max power condition should change in time. Thus, a photovoltaic system normally equips a MPPT system. In standard MPPT systems, they are programmed based on a hill-climbing method (sweeping the voltage so that the output power should increase at each iteration step). Let us consider a case where the MPPT is performed in a HCSC with a I-V curve, as shown in

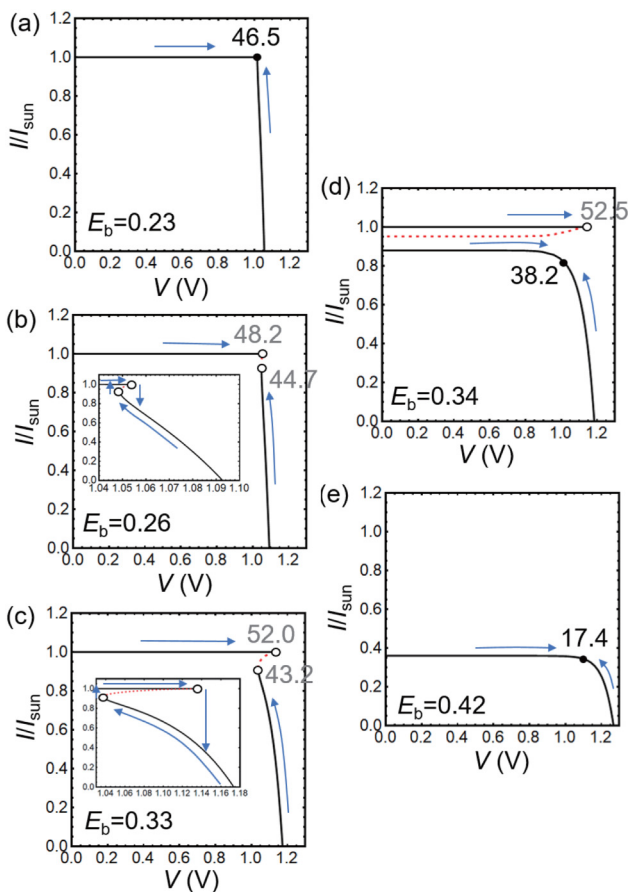


FIG. 4. I-V curves for different E_b 's: (a) 0.23 eV, (b) 0.26 eV, (c) 0.33 eV, (d) 0.34 eV, and (e) 0.42 eV (we set $E_g = 0.93 \text{ eV}$, $\text{CR} = 1000$, $w = 100 \text{ nm}$, $\Delta E = 0.1 \text{ eV}$, $\tau_{\text{th}} = 1 \text{ ns}$, $\tau_{\text{eq}} = 1 \text{ ps}$, and $\tau_{\text{out}} = 10^{-11} \text{ s}$). The MPPs, both in the upper and lower branches, are shown by circles with η_{\max} indicated. Results of linear (Lyapunov) stability analysis are also shown in the plot: stable curves by black solid lines, unstable curves by red dashed lines, stable MPPs by filled circles, and unstable MPPs by open circles. Arrows on the I-V curves indicate the directions of the MPP trucking by a hill-climbing method at each point. Insets in the figures are magnified views of a part of the I-V curves.

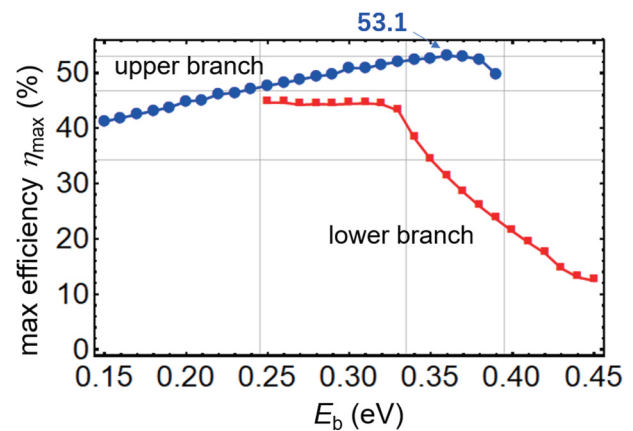


FIG. 5. η_{\max} at MPPs in the upper and lower branches of the I-V curves are plotted as a function of E_b (we set $E_g = 0.93 \text{ eV}$, $\text{CR} = 1000$, $w = 100 \text{ nm}$, $\Delta E = 0.1 \text{ eV}$, $\tau_{\text{th}} = 1 \text{ ns}$, $\tau_{\text{eq}} = 1 \text{ ps}$, and $\tau_{\text{out}} = 10^{-11} \text{ s}$). η_{\max} corresponds to an unstable MPP for $E_b \geq 0.25 \text{ eV}$ in the upper branch and for $E_b \leq 0.33 \text{ eV}$ in the lower branch (see the text explanation for details).

Figs. 4(a)–4(e) (tracking starts at the short-circuit condition at a branch with larger I , and arrows in the figures indicate the direction at each point). The MPPT history is shown in Fig. 6 [η vs time (iteration step)]. When the I–V curve has a stable MPP ($E_b = 0.23, 0.34, 0.42$ eV in Fig. 4), η reaches a single MPP finally after the MPPT, as shown in Figs. 6(a), 6(d), and 6(e). Therefore, η_{\max} at the stable MPP is identical to the long-time-averaged efficiency in the presence of the MPPT: 46.5, 38.2, 17.4% for Figs. 4(a), 4(d), and 4(e), respectively. On the other hand, in cases when the I–V curve has two unstable MPPs [$E_b = 0.26, 0.33$ eV in Figs. 4(b) and 4(c)], the MPPT does not end with a single η but oscillates endlessly between the max value at the upper branch and the lower value at the lower branch of the I–V curves, as shown in Figs. 6(b) and 6(c). As a result, the long-time-averaged efficiency decreases significantly from the η_{\max} in the upper branch. In Fig. 7, the long-time-averaged efficiency given by the MPPT, is plotted by a filled circle overlaid onto Fig. 5, clarifying that a HCSC with the MPPT system has the maximum efficiency 47.1% with a smaller optimal $E_b (=0.24$ eV) largely reduced from the maximum value 53.1% at the unstable MPP with $E_b = 0.36$ eV (upper branch). At this point, we should remind that this instability and a reduction in η_{\max} occurs even though the illumination condition is being fixed.

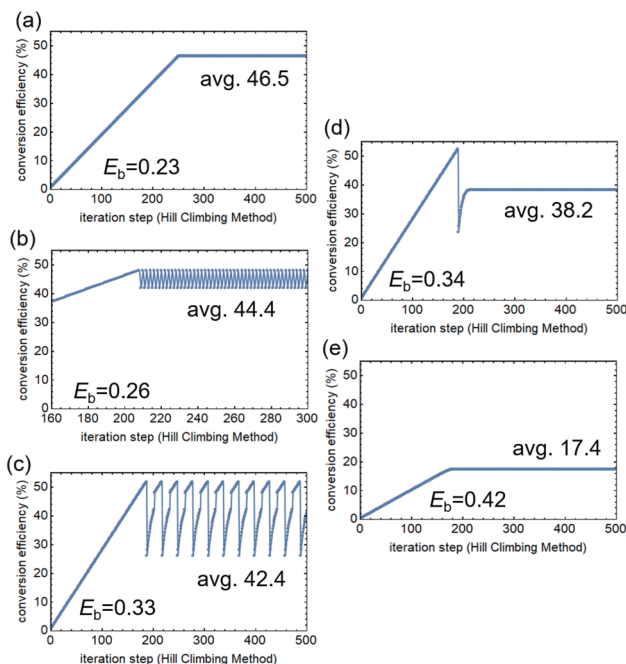


FIG. 6. Histories of the MPP tracking with a hill-climbing method (η vs iteration step) are simulated for HCSCs with different I–V curves: E_b = (a) 0.23 eV, (b) 0.26 eV, (c) 0.33 eV, (d) 0.34 eV, and (e) 0.42 eV (we set $E_g = 0.93$ eV, $CR = 1000$, $w = 100$ nm, $\Delta E = 0.1$ eV, $\tau_{th} = 1$ ns, $\tau_{eq} = 1$ ps, and $\tau_{out} = 10^{-11}$ s). In all the simulation, iteration starts from $V = 0$ at a branch with a larger I in Fig. 4. After a sufficient time evolution, a MPP tracking eventually reaches a stable MPP or shows a periodic behavior. The long-time-averaged η is indicated in each panel.

Figure 3 shows both the long-time-averaged max efficiency (black, filled circle) and η_{\max} in the upper branch (gray, filled square) are determined in this way.

Of course, other MPPT algorithms³³ different from the hill-climbing method could be considered in order to avoid the periodic behavior. For example, the MPP could be determined by measuring a full I–V curve by sweeping the voltage in both forward and reverse directions between $V = 0$ and $V = V_{oc}$ [and also by selecting an approximate maximum at a certain distance apart from the true MPP if the I–V curves are similar to Figs. 4(b)–4(d)]. However, such an algorithm obviously complicates the MPPT system and enlarges the response time. This could cause a delay from time-varying illumination conditions leading to a power loss in real application.

The second example of the instabilities will occur in a module consisting of plural HCSCs, in which they are connected electrically in series. Series connection is normally preferred in photovoltaic modules in order to avoid an increase in the resistive loss, since the total current does not increase with the number of cells while the output voltage increases instead. On the other hand, an increase in the resistive loss for a large number of cells is unavoidable with a parallel connection. However, for a series connection, the output currents from different HCSCs must coincide with each other (i.e., a current matching is required for all HCSCs in a module). If one considers a fact that I_{sc} in real devices can deviate on a device-by-device basis for certain reasons (e.g., the light trapping properties, bulk and surface recombination properties, thickness, and illumination condition will be different for different devices), the upper branch of the I–V curves in Figs. 4(b)–4(d) cannot be used for a module, since the exact current matching at the single value of $I/I_{sun} = 1.0$ seems impossible. If the HCSCs with I–V curves in Figs. 4(b)–4(d) are used in a module, the current matching for series connection can be available only for the lower branch of the I–V curves, which will significantly decrease the device

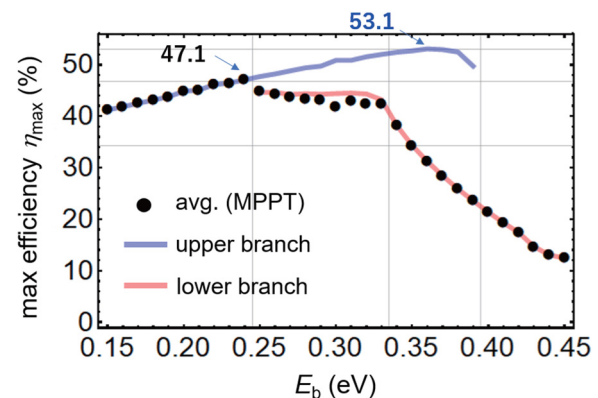


FIG. 7. η_{\max} as a long-time-averaged efficiency by the MPPT (filled circles) plotted as a function of E_b (we set $E_g = 0.93$ eV, $CR = 1000$, $w = 100$ nm, $\Delta E = 0.1$ eV, $\tau_{th} = 1$ ns, $\tau_{eq} = 1$ ps, and $\tau_{out} = 10^{-11}$ s). The plot is overlaid onto Fig. 5; opaque curves in blue and red correspond to the upper and lower branches in Fig. 5, respectively.

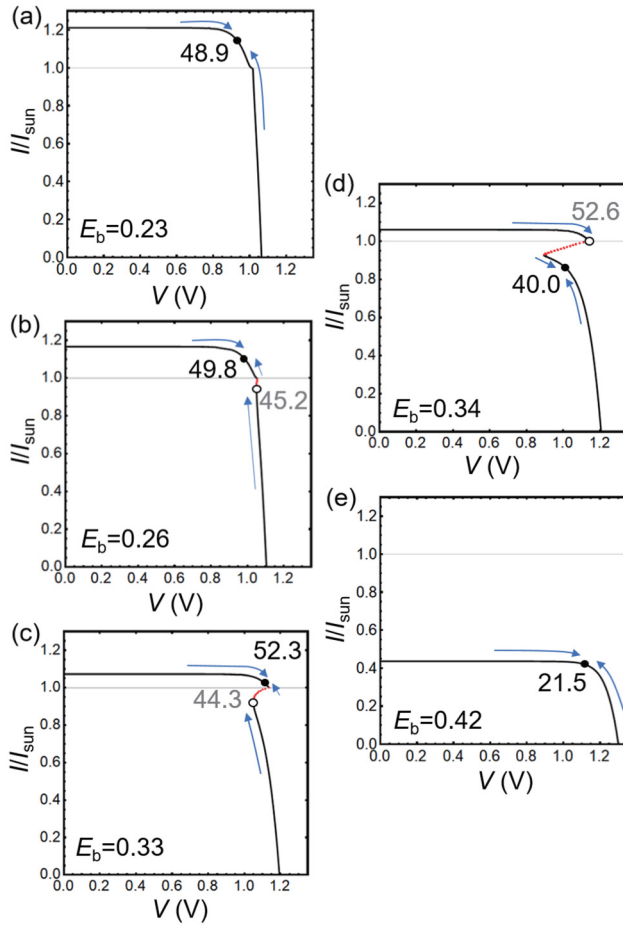


FIG. 8. I-V curves for different E_b 's in the presence of II and AR effects with $C_{AR} = 10^{-28} \text{ cm}^6/\text{s}$: (a) 0.23 eV, (b) 0.26 eV, (c) 0.33 eV, (d) 0.34 eV, and (e) 0.42 eV (we set $E_g = 0.93 \text{ eV}$, $CR = 1000$, $w = 100 \text{ nm}$, $\Delta E = 0.1 \text{ eV}$, $\tau_{th} = 1 \text{ ns}$, $\tau_{eq} = 1 \text{ ps}$, and $\tau_{out} = 10^{-11} \text{ s}$). The MPPs, both in the upper and lower branches, are shown by circles with the η_{max} indicated. Results of linear (Lyapunov) stability analysis are also shown in the plot: stable curves by black solid lines, unstable curves by red dashed lines, stable MPPs by filled circles, and unstable MPPs by open circles. Arrows on the I-V curves indicate the directions of the MPP trucking by a hill-climbing method at each point.

efficiency in a module (at least to a value lower than the lower branch in Fig. 5). As a result, when considering the efficiency as a module, η_{max} will be maximized at most to 47.1% with the smaller value of $E_b = 0.24 \text{ eV}$ (with a continuous I-V curve), which is the same η_{max} as that found for a case of the first example of the instabilities in a HCSC with a MPPT system (Fig. 7).

B. Effects of impact ionization (II) and Auger recombination (AR)

As stated in the Introduction, it is pointed out by Würfel *et al.*⁹ that inclusion of particle-number non-conserving processes,

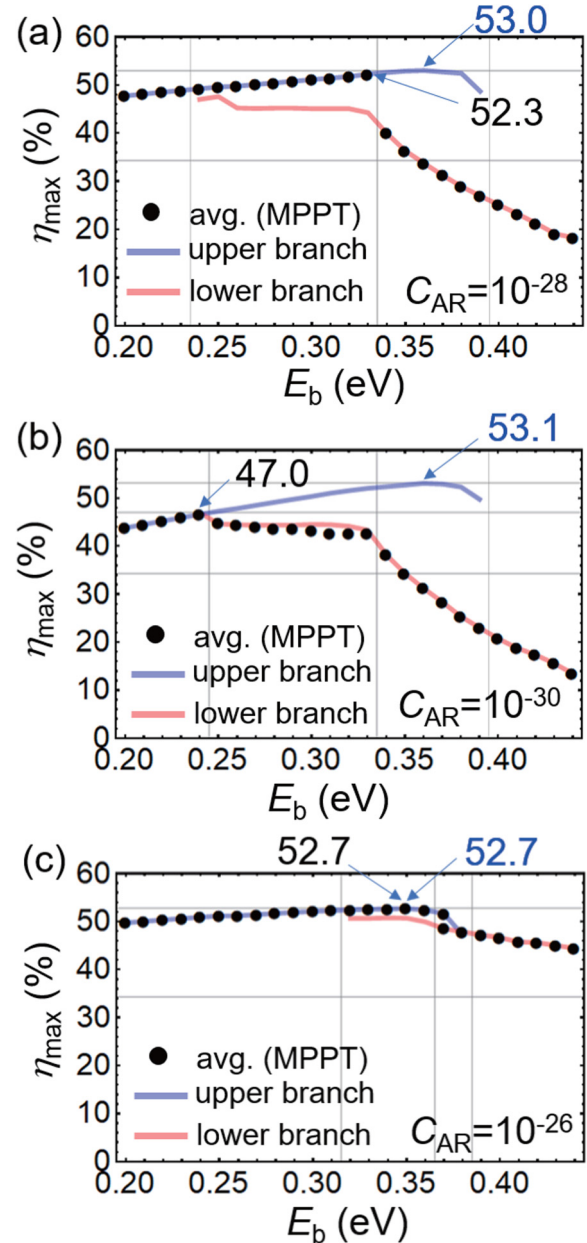


FIG. 9. η_{max} as a long-time-averaged efficiency by the MPPT (filled circles) plotted as a function of E_b , in presence of II and AR effects: $C_{AR} =$ (a) $10^{-28} \text{ cm}^6/\text{s}$, (b) $10^{-30} \text{ cm}^6/\text{s}$, (c) $10^{-26} \text{ cm}^6/\text{s}$ (we set $E_g = 0.93 \text{ eV}$, $CR = 1000$, $w = 100 \text{ nm}$, $\Delta E = 0.1 \text{ eV}$, $\tau_{th} = 1 \text{ ns}$, $\tau_{eq} = 1 \text{ ps}$, and $\tau_{out} = 10^{-11} \text{ s}$). Blue and red opaque curves are η_{max} in the upper and lower branches obtained in the same manner as Figs. 5 and 7.

e.g., II and AR processes, is necessary to obtain reliable I-V curves in hot-carrier solar cells (especially at the short-circuit condition). The particle-number conserving (PC) model without II and AR processes¹ can give a smooth but physically meaningless I-V curve

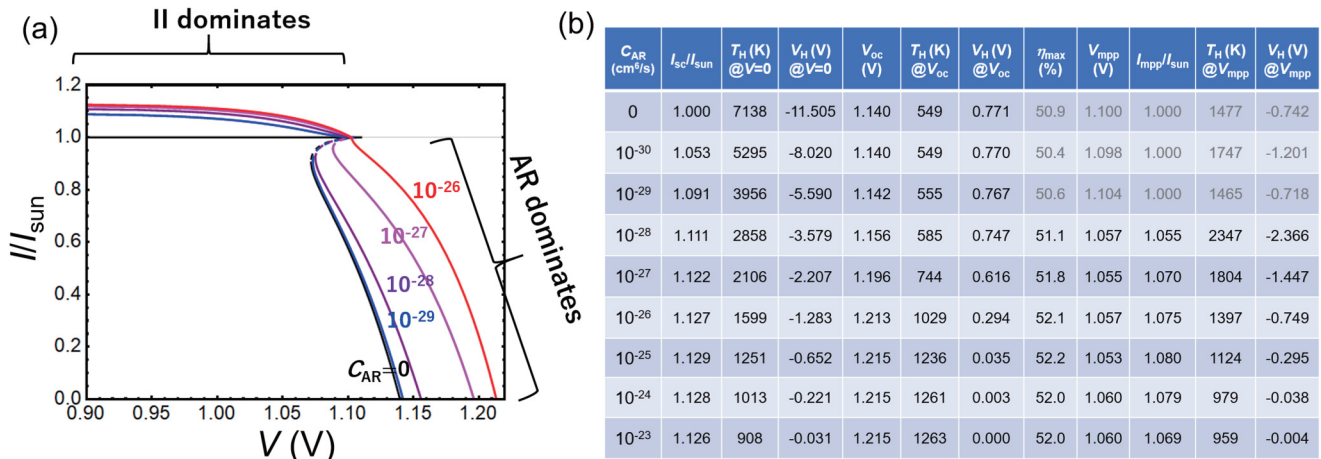


FIG. 10. (a) I-V curves plotted in the presence of II and AR effects with different values of C_{AR} ($= 0, 10^{-29}, 10^{-28}, 10^{-27},$ and 10^{-26} cm⁶/s) and (b) list of the I-V parameters for $0 \leq C_{AR} \leq 10^{-23}$ cm⁶/s, in which the hot-carrier temperature, T_H , and the Fermi-level separation of the hot carriers, V_H , at short-circuit, open-circuit, max power conditions ($V = 0, V_{oc}$, and V_{mpp}) are also given. V_H is given by μ_H via $\mu_H = (qV_H - E_g)/2$. η_{max} is the maximum efficiency in the I-V curve whose values are given in black (gray) numbers for stable (unstable) MPPs (see also Fig. 11). We set $E_b = 0.3$ eV, $E_g = 0.93$ eV, $CR = 1000$, $w = 100$ nm, $\Delta E = 0.1$ eV, $\tau_{th} = 1$ ns, $\tau_{eq} = 1$ ps, and $\tau_{out} = 10^{-11}$ s.

with an extremely high T_H sensitive to V . On the other hand, Würfel³⁴ considered an opposite limit where II and AR processes are the fastest among all dynamics of the hot carriers. This latter limit is described by assuming the Fermi-level separation of the hot carriers to be zero, i.e., $V_H = 0$,³⁴ which gives a smooth and physically meaningful I-V curve. We consider a real HCSC is situated between the two limits. The intermediate case between the two limits can be parametrized by an Auger recombination coefficient of the absorber, C_{AR} , as explained below.

In this section, we include the effect of II and AR processes in the rate equations given in Sec. II, by adding a term due to II and AR, $\mathcal{R}_E^{II-AR} (= \mathcal{R}_E^{II} + \mathcal{R}_E^{AR})$, to Eq. (1). Since II and AR processes originate from carrier-carrier scattering (direct Coulomb³⁵ and/or indirect phonon-mediated Coulomb scattering³⁶), strict treatment of them is not an easy task (even the lowest-order perturbation theory requires integration over Coulomb scattering matrix with total momentum and energy conservation being kept³⁵). However, inclusion of II and AR processes to our rate equation model becomes much easier by adopting a constant for the scattering matrix element and relaxing the momentum conservation with only the energy conservation being kept (see the Appendix for the derivation of \mathcal{R}_E^{II-AR}). We consider the relaxed momentum conservation is a reasonable assumption in some cases³⁶ (e.g., in the case of phonon-mediated Coulomb scattering, or in amorphous, nano-crystal, and quasi-crystal materials without translational symmetry) and such a treatment will not lose the essence of II and AR processes. The essence will be that the carrier temperature should decrease by increasing the number of electron-hole pairs in II and vice versa in AR.

Here, we present a numerical study based on such an effective theory. In this theory, an established material-dependent parameter, an Auger coefficient C_{AR} (cm⁶/s), is used as a single parameter

indicating the strength of II and AR processes (related to the constant for the scattering matrix element). As shown below, $C_{AR} = 0$ corresponds to the PC model used in Subsection III A, and $C_{AR} = +\infty$ describes a limiting situation considered in the Würfel's model (with $V_H = 0$).³⁴ What we shall focus here is how the results for the I-V curves and the stability in Sec. III A (with $C_{AR} = 0$) could be modified in real HCSCs with a realistic value of C_{AR} , and how much the previous two limiting models (PC and Würfel's models) can describe the properties of real HCSCs.

Figure 8 show the I-V curves under the effect of II and AR with $C_{AR} = 10^{-28}$ cm⁶/s for different values of E_b [(a)–(e)]. Figures 8(a)–8(e) and Figs. 4(a)–4(e) can be compared directly since they use the same parameters except for C_{AR} . In I-V curves in Fig. 8 ($C_{AR} > 0$), it is clear that the short-circuit current I_{sc} becomes larger than those in Fig. 4 ($C_{AR} = 0$) and I_{sc}/I_{sun} exceeds unity for $E_b \leq 0.34$ eV [(a)–(d)]. This indicates II (carrier multiplication) dominates AR at the short-circuit condition, since $I_{sc}/I_{sun} > 1$ means that the number of electron-hole pairs output to the electrodes is larger than the number of photons absorbed. For $E_b \leq 0.34$ eV [(a)–(d)], I/I_{sun} continuously decreases with V and reaches unity at a certain V , where the I-V curves have a corner and the stable upper branch merges with an unstable middle branch (with a negative differential resistance) for $0.26 \leq E_b \leq 0.34$ [(b)–(d)]. As I/I_{sun} decreases below unity, the unstable middle branch changes to a stable branch (with a positive differential resistance), which continues to the open-circuit point $I/I_{sun} = 0$. With increasing E_b further from 0.34 eV to 0.42 eV [from (d) to (e)], the upper stable and middle unstable branches disappear at a certain value of E_b while the lower stable branch changes continuously to have larger V_{oc} and smaller I_{sc} . The overall features of the I-V curves in Fig. 8 are similar to those found in Fig. 4, except that I_{sc}/I_{sun} can exceed unity.

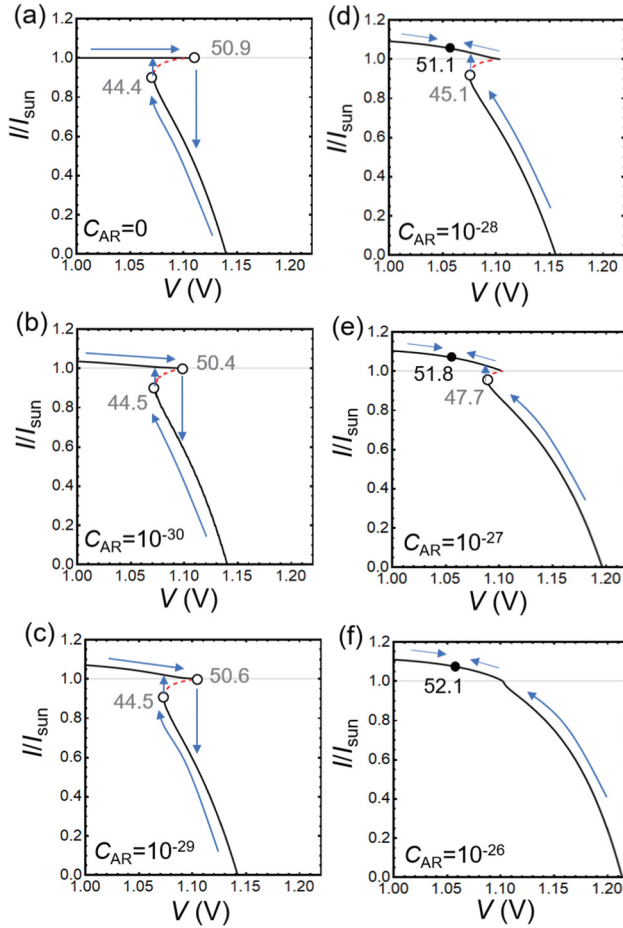


FIG. 11. I-V curves plotted in the presence of II and AR effects with different values of C_{AR} : (a) 0, (b) 10^{-30} , (c) 10^{-29} , (d) 10^{-28} , (e) 10^{-27} , and (f) 10^{-26} cm^6/s [magnified views of the curves in Fig. 10(a)]. We set $E_b = 0.3$ eV, $E_g = 0.93$ eV, $CR = 1000$, $w = 100$ nm, $\Delta E = 0.1$ eV, $\tau_{th} = 1$ ns, $\tau_{eq} = 1$ ps, and $\tau_{out} = 10^{-11}$ s. Black solid lines and red dashed lines are Lyapunov stable and unstable according to the linear stability analysis. Filled and open circles are the stable and unstable MPPs in the upper and lower branches. The values of η_{max} are indicated at each MPP. Arrows indicate the direction of MPP trucking at each point.

However, there are important differences related to the operational stability. Since the stable upper branch has a finite range in I/I_{sun} ($1 \leq I/I_{sun} \leq I_{sc}/I_{sun}$), the MPPs in the upper branch can leave the edges at $I/I_{sun} = 1$, if I_{sc}/I_{sun} exceeds a certain value [Figs. 8(a)–8(c)]. As a result, the MPP in the upper branch can be stable even if a MPP trucking was performed in Figs. 8(a)–8(c); e.g., η_{max} can be 52.3% in a stable operation for (c) $E_g = 0.33$ eV. This means that II and AR effects reduce the dynamic instability in the efficient HCSCs (instability of the first example in Sec. III A). Moreover, a finite range in the upper branch ($1 \leq I/I_{sun} \leq I_{sc}/I_{sun}$) means that the upper branch in the I-V curve could be utilized in a module of series-connected

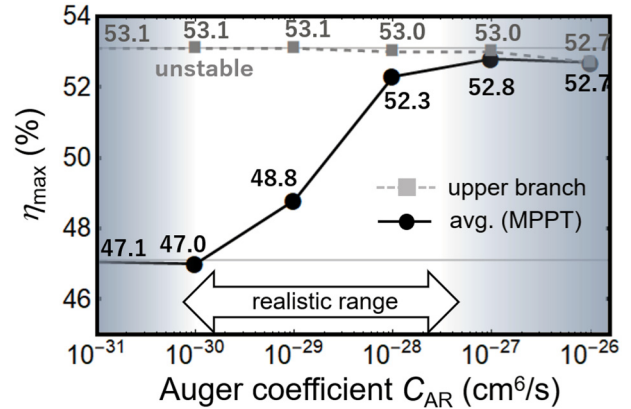


FIG. 12. η_{max} as a function of the Auger coefficient C_{AR} obtained by optimizing V and E_b (we set $E_g = 0.93$ eV, $CR = 1000$, $w = 100$ nm, $\Delta E = 0.1$ eV, $\tau_{th} = 1$ ns, $\tau_{eq} = 1$ ps, and $\tau_{out} = 10^{-11}$ s). Black filled circles are η_{max} as a long-time-averaged efficiency by the MPPT, and gray squares are η_{max} at the MPPs in the upper branch of I-V curves (unstable for $C_{AR} \leq 10^{-27}$ cm^6/s). For semiconductors with $E_g = 0.93$ eV, a realistic range of C_{AR} is between 10^{-30} and 10^{-27} cm^6/s (white region; see, e.g., Fig. 3.12 of Ref. 37).

plural HCSCs with non-uniform I_{sc} , even though a finite gap exists between the upper and lower branches [Figs. 8(b)–8(c)]. Therefore, II and AR effects reduce also the instability of the second example in Sec. III A.

In Fig. 9, we plotted η_{max} as a long-time-averaged efficiency by the MPP trucking (hill-climbing method) as a function of E_b (black filled circles) for $C_{AR} =$ (a) 10^{-28} cm^6/s , (b) 10^{-30} cm^6/s , (c) 10^{-26} cm^6/s . The plots are overlaid on other curves for η_{max} at the MPPs in the upper and lower branches of the I-V curves (blue and red opaque curves). These results are compared with Fig. 7 (with $C_{AR} = 0$). The result for $C_{AR} = 10^{-30}$ cm^6/s [Fig. 9(b)] is almost the same as that for $C_{AR} = 0$ (Fig. 7). As increasing II and AR effects [with a larger C_{AR} in Figs. 9(a) and 9(c)], some changes are clearly found. The long-time-averaged value of η_{max} (black filled circles) starts to overlap with the upper branch curve (blue opaque) for a wider range of E_b with a larger C_{AR} . This result reflects the above-mentioned reduction in the dynamic instability of the MPP in the upper branch due to II and AR effects. It is also an interesting feature that the E_b -dependency of η_{max} becomes weaker as C_{AR} increases while the maximum value of η_{max} in the upper branch is almost unchanged ($13.5 \leq \eta_{max}(\%) \leq 53.1$ for $C_{AR} = 10^{-30}$ cm^6/s , $18.3 \leq \eta_{max} \leq 53.0$ for $C_{AR} = 10^{-28}$ cm^6/s , and $44.5 \leq \eta_{max} \leq 52.7$ for $C_{AR} = 10^{-26}$ cm^6/s in Fig. 9). This is consistent with the result of Würfel's model (corresponds to the limit $C_{AR} = +\infty$) by which η_{max} has no dependency on the energy level of the carrier extraction.³⁴

In Figs. 10(a) and 10(b), we show the dependency of the I-V curves and the I-V parameters on C_{AR} with E_b being fixed at 0.3 eV. As C_{AR} increases from zero, the I-V curve with a sharp corner at $I/I_{sun} = 1$ and a hysteresis characteristic changes gradually and becomes smooth for $C_{AR} \leq 10^{-26}$ cm^6/s [Fig. 10(a)]. Throughout the change, both I_{sc} and V_{oc} increase with C_{AR} while

η_{\max} does not change so much, as seen clearly in the table of I–V parameters [Fig. 10(b)]. These results can be understood by the expression of II and AR rates, $R_E^{\text{II-AR}}$, and the nature of II and AR processes. We found $V_H < 0$ near the short-circuit condition with $I/I_{\text{sun}} > 1$, whereas $V_H > 0$ near the open-circuit condition [Fig. 10(b)]. This means II dominates AR (i.e., $R_E^{\text{II-AR}} > 0$) near the short-circuit condition and vice versa (i.e., $R_E^{\text{II-AR}} < 0$) near the open-circuit condition since $R_E^{\text{II-AR}} \propto (1 - e^{qV_H/k_B T_H})$ [see Eq. (A5) in the Appendix]. II increases the number of carriers to be extracted by reducing the kinetic energy and temperature T_H of the hot carriers, thus increases I_{sc} , while AR increases the kinetic energy and temperature T_H of hot carriers by reducing the number of carriers, thus increases V_{oc} . II and AR effects are balanced and canceled with each other at $V_H = 0$, which occur near the MPPs located between the short-circuit and open-circuit conditions. As a result, η_{\max} at the MPPs has a weak dependency on C_{AR} . These explanations are supported by the data in Fig. 10(b). It should also be noted that this model smoothly interpolates the results of the PC model (characterized by a negative V_H and a high T_H with $C_{\text{AR}} = 0$) and Würfel's model (characterized by $V_H = 0$ and smooth I–V curve at $C_{\text{AR}} = +\infty$).

The magnified views of the I–V curves are shown in Fig. 11, where the operational stability at each point is also indicated, and the stable and unstable MPPs are shown by filled and open circles. As found clearly, while the MPPs in the upper and lower branches are unstable for $C_{\text{AR}} \leq 10^{-29} \text{ cm}^6/\text{s}$ [Figs. 11(a)–11(c)], the MPP in the upper branch becomes stable for $C_{\text{AR}} \geq 10^{-28} \text{ cm}^6/\text{s}$ [Figs. 11(d)–11(f)]. This means the operation of a HCSC, which is unstable for a small $C_{\text{AR}} \leq 10^{-29} \text{ cm}^6/\text{s}$, can be stable for a large $C_{\text{AR}} \geq 10^{-28} \text{ cm}^6/\text{s}$ given the absorber is made of a semiconductor with $E_g = 0.93 \text{ eV}$. In Fig. 12, we showed a long-time-averaged η_{\max} (by the MPPT) as a function of C_{AR} . The long-time-averaged η_{\max} increases with C_{AR} and almost saturated close to the η_{\max} in the upper branch for $C_{\text{AR}} \geq 10^{-28} \text{ cm}^6/\text{s}$, meaning that the MPP in the upper branch of I–V curves becomes stable for $C_{\text{AR}} \geq 10^{-28} \text{ cm}^6/\text{s}$. Therefore, we can conclude that $C_{\text{AR}} \geq 10^{-28} \text{ cm}^6/\text{s}$ is a requirement for a stable operation of the highly efficient HCSCs (with $\eta_{\max} > 50\%$) with $E_g = 0.93 \text{ eV}$. The condition could be reached in real devices, since C_{AR} ranges between $10^{-30} \text{ cm}^6/\text{s}$ and $10^{-27} \text{ cm}^6/\text{s}$ in a semiconductor material with $E_g = 0.93 \text{ eV}$ (see, e.g., Fig. 3.12 of Ref. 37).

In the end of this section, we would like to give an intuitive explanation on the physics and the origin of the instability and multibranch I–V curves in relation to II and AR processes. As found in Fig. 10(b), T_H is high at a short-circuit condition since the back-flow of cold carriers from the contacts into the absorber is negligible. On the other hand, at an open-circuit condition, the back-flow of the cold carriers cannot be negligible, and the injected cold carriers reduces T_H by the interaction with the hot carriers already present in the absorber. Roughly speaking, we can consider that the I–V curve of a HCSC is consisting of two parts: one with a larger T_H at $V < V_{\text{mpp}}$ and the other with a lower T_H at $V > V_{\text{mpp}}$. Therefore, an efficient hot-carrier solar cell operation (with a high T_H at a large V) is inherently unstable unless efficient II–AR processes are present. Frequent II–AR processes exchange the total number and the total kinetic energy (the hot-

carrier temperature) of the carriers, moderating the sharp change in T_H around the MPP and giving an operational stability to a HCSC. Notice that an efficient HCSC equips high-energy-selective barriers, which reduce the back-flow of the cold carriers in the electrodes (by which a large V_{oc} is available). The carriers with a larger T_H can leap the barriers at a higher probability than those with a lower T_H do. As a result, two values of the current in the I–V curves at a given V in (for a certain range of E_b): one with larger I and T_H and the other with smaller I and T_H . This is the origin of the multibranch I–V curves.

IV. CONCLUSIONS

In this paper, we studied the I–V curves and the operational stability of the steady-state operation in HCSCs, based on the non-equilibrium theory that takes into account the realistic time-scales of the hot-carrier dynamics. The effects of impact ionization (II) and Auger recombination (AR) of hot carriers are also investigated. We found that an efficient HCSC shows a hysteresis behavior in the I–V curve and focused two types of instabilities related to the hysteresis; one is intrinsic in a single cell and the other arises when plural cells are series-connected. To avoid the instability, we need to choose a smaller energy level for the carrier extraction (a smaller E_b), which, in turn, results in reduction in the real-device efficiency (a time-averaged or a module efficiency) if there are no II and AR effects. On the other hand, II and AR effects are shown to stabilize the operation and increase the real-device efficiency if an absorber has a large AR coefficient ($\eta_{\max} > 50\%$ if $C_{\text{AR}} \geq 10^{-28} \text{ cm}^6/\text{s}$ for $E_g = 0.93 \text{ eV}$). We can summarize these results to an important design guide for a stable and efficient HCSC; *a semiconductor with a larger AR coefficient should be selected as the light absorber.*

In the literature not only on HCSCs, we found only a few theoretical investigations on the operational stability in solar cells.³⁸ This is in contrast with studies on lasers whose dynamics are often investigated as a typical example of nonlinear dynamical systems (the difference seems to come from the difference in the timescales of the operation, i.e., solar cells are aimed for a steady-state operation).^{32,39} However, the application of the similar stability analysis to other types of solar cells (those based on novel materials like perovskite solar cells, and other advanced-concept devices such as intermediate-band⁴⁰ and heat-recovery⁴¹ solar cells) can bring us a new knowledge toward realization of more efficient and more stable photovoltaic systems.

ACKNOWLEDGMENTS

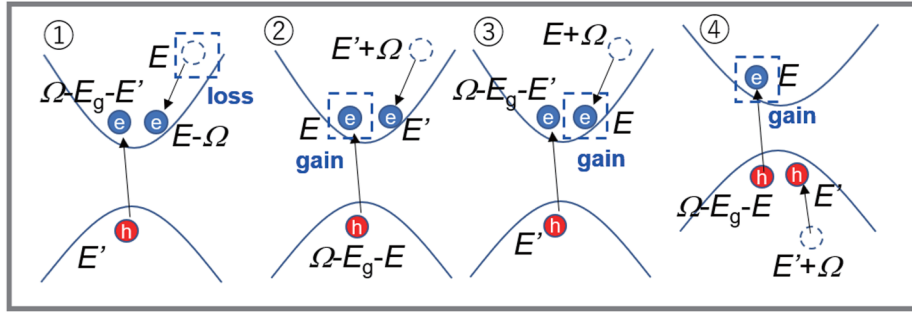
The author thanks Y. Takeda, H. Akiyama, T. Mochizuki, and H. Takato for discussion. This work was supported by JSPS KAKENHI Grant Number JP19K04523.

APPENDIX: DERIVATION OF II-AR RATE $\mathcal{R}_E^{\text{II-AR}}$

In Sec. III B, we incorporated the effects of II and AR processes by adding the corresponding term $\mathcal{R}_E^{\text{II-AR}} (= \mathcal{R}_E^{\text{II}} + \mathcal{R}_E^{\text{AR}})$ in the rate Eq. (1). Here, we describe a derivation of $\mathcal{R}_E^{\text{II-AR}}$.

They are given by the second-order perturbation theory with respect to the carrier–carrier interaction (the Coulomb interaction).

(a) Impact Ionization (II) Processes



(b) Auger Recombination (AR) Processes

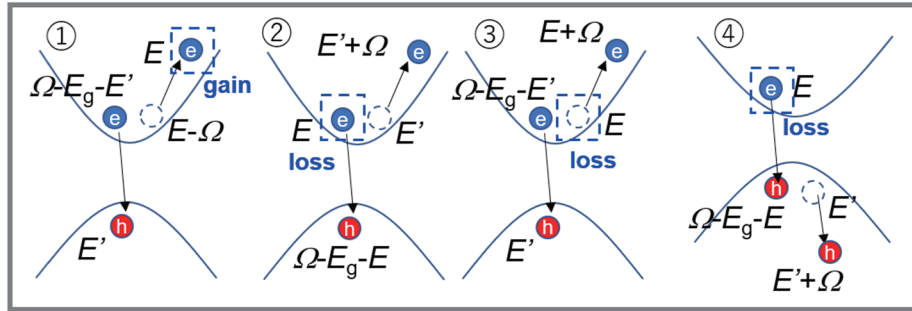


FIG. 13. Schematic images of (a) impact ionization (II) and Auger recombination (AR) processes, corresponding to the terms in Eqs. (A1) and (A2), respectively. Energies of electrons and holes are measured, respectively, from the conduction- and valence-band edges.

As mentioned in Sec. III B, we made following simplifications to obtain the final results. We treat the matrix element for the carrier-carrier interaction as a constant (included as constants W_e and W_h below), and for the sake of simplicity, we computed the rate by relaxing the momentum conservation³⁶ while the

energy conservation is being kept (which is allowed for the case of phonon-assisted processes or for absorber's materials without a translational symmetry). Adopting these simplifications, we have the following expressions for the II and AR rates for the rate equation:

$$\begin{aligned} \mathcal{R}_E^{\text{II}} = & -W_e \int_{E_g}^E \left(\int_0^{\Omega-E_g} n_E^e \mathcal{D}_e(E-\Omega) \mathcal{D}_e(\Omega-E_g-E') \mathcal{D}_h(E') dE' \right) d\Omega + W_e \int_{E_g+E}^{\infty} \left(\int_0^{\infty} n_{E'+\Omega}^e \mathcal{D}_e(E'+\Omega) \mathcal{D}_e(E') \mathcal{D}_h(\Omega-E_g-E) dE' \right) d\Omega \\ & + W_e \int_{E_g}^{\infty} \left(\int_0^{\Omega-E_g} n_{E+\Omega}^e \mathcal{D}_e(E+\Omega) \mathcal{D}_e(\Omega-E_g-E') \mathcal{D}_h(E') dE' \right) d\Omega + W_h \int_{E_g+E}^{\infty} \left(\int_0^{\infty} n_{E'+\Omega}^h \mathcal{D}_h(E') \mathcal{D}_h(E'+\Omega) \mathcal{D}_h(\Omega-E_g-E) dE' \right) d\Omega, \end{aligned} \quad (\text{A1})$$

$$\begin{aligned} \mathcal{R}_E^{\text{AR}} = & W_e \int_{E_g}^E \left(\int_0^{\Omega-E_g} n_{E-\Omega}^e n_{\Omega-E_g-E'}^e n_{E'}^h \mathcal{D}_e(E-\Omega) \mathcal{D}_e(\Omega-E_g-E') \mathcal{D}_h(E') dE' \right) d\Omega \\ & - W_e \int_{E_g+E}^{\infty} \left(\int_0^{\infty} n_E^e n_{E'}^e n_{\Omega-E_g-E}^h \mathcal{D}_e(E'+\Omega) \mathcal{D}_e(E') \mathcal{D}_h(\Omega-E_g-E) dE' \right) d\Omega \\ & - W_e \int_{E_g}^{\infty} \left(\int_0^{\Omega-E_g} n_E^e n_{\Omega-E_g-E'}^e n_{E'}^h \mathcal{D}_e(E+\Omega) \mathcal{D}_e(\Omega-E_g-E') \mathcal{D}_h(E') dE' \right) d\Omega \\ & - W_h \int_{E_g+E}^{\infty} \left(\int_0^{\infty} n_E^h n_{\Omega-E_g-E}^h n_{E'}^h \mathcal{D}_h(E') \mathcal{D}_h(E'+\Omega) \mathcal{D}_h(\Omega-E_g-E) dE' \right) d\Omega. \end{aligned} \quad (\text{A2})$$

Terms in the right-hand side of Eqs. (A1) and (A2) originate from the II and AR processes, schematically shown in Figs. 13(a) and 13(b), respectively. For the sake of clarity, here we used different notations for the carrier distribution functions for electrons and holes, n_E^e and n_E^h , while we notice that they are equivalent in our model with an electron-hole symmetry. The same applies also to the scattering matrix: W_e for electrons and W_h for holes, while they are equivalent.

Direct use of Eqs. (A1) and (A2) in the rate equation should give numerical solutions to the steady states, since the rate equation is a closed set of the distribution function. However, we cannot use a simple analytic solution as those found in Eq. (7) for further analysis, since the term $\mathcal{R}_E^{\text{AR}}$ is a cubic function of n_E .

Instead of using the exact form in Eqs. (A1) and (A2), we make an approximation in Eqs. (A1) and (A2), which enables us to obtain an analytic solution for n_E . As mentioned in Sec. II B, the carrier distribution function can be approximated by the Fermi-Dirac distribution function, $f_{\mu_H, T_H}(E)$, if the equilibration time τ_{eq} is much faster than any other timescales in the HCSC. This is true, and the approximation is valid in our simulation. Another validation of this approximation is that, because the rates in Eqs. (A1) and (A2) are given as integrals over E , they are not sensitive to a small deviation in n_E , which is found in an energy window of the carrier extraction ($E_b < E < E_b + \Delta E$) according to Eq. (7). This observation allows us to replace n_E in Eqs. (A1) and (A2) by $f_{\mu_H, T_H}(E)$ with representative values of μ_H and T_H . Inserting $n_E^{(h)} = f_{\mu_H, T_H}(E) \approx \exp(-(E - \mu_H)/k_B T_H)$ to Eqs. (A1) and (A2), we find the rates, $\mathcal{R}_E^{\text{II}}$, $\mathcal{R}_E^{\text{AR}}$, and $\mathcal{R}_E^{\text{II-AR}}$, as a function of $\mu_H (= (qV_H - E_g)/2)$ and T_H ,

$$\mathcal{R}_E^{\text{II}} = W d_e^3 \left(-\frac{2\pi}{105} (E - E_g)^{7/2} \exp(-(E - \mu_H)/(k_B T_H)) \times \theta(E - E_g) + \frac{3\pi}{8} (k_B T_H)^{7/2} \exp(-(E + E_g - \mu_H)/(k_B T_H)) \times g_1(E/(k_B T_H)) \right), \quad (\text{A3})$$

$$\mathcal{R}_E^{\text{AR}} = -\exp(qV_H/(k_B T_H)) \times \mathcal{R}_E^{\text{II}}, \quad (\text{A4})$$

$$\mathcal{R}_E^{\text{II-AR}} = (1 - \exp(qV_H/(k_B T_H))) \times \mathcal{R}_E^{\text{II}}, \quad (\text{A5})$$

where $\theta(x)$ is unit step function and $g_1(x) \equiv \int_0^{+\infty} z^2 \sqrt{z+x} e^{-z} dz$. We used the electron-hole symmetry in the present model, $W_e = W_h = W$ and $\mathcal{D}_e(E) = \mathcal{D}_h(E) = d_e \sqrt{E}$ to obtain the final expressions.

Based on the expressions in Eq. (A4) with (A3), we can relate the scattering constant $W (= W_e = W_h)$ to an AR coefficient C_{AR} as follows. The rate equation for the total carrier density N is given by integrating Eq. (1) over all energy states. Therefore, the AR loss rate for N is given by

$$\left. \frac{dN}{dt} \right|_{\text{AR}} = -C_{\text{AR}} N^3 = \int_0^\infty \mathcal{D}_e(E) \times \mathcal{R}_E^{\text{AR}} dE, \quad (\text{A6})$$

where we used a definition of an AR coefficient C_{AR} in the first equation, and

$$N = \int_0^\infty \mathcal{D}_e(E) \times n_E dE \approx \int_0^\infty \mathcal{D}_e(E) \times \exp(-(E - \mu_H)/k_B T_H) dE. \quad (\text{A7})$$

Combining Eqs. (A6) and (A7), and using Eqs. (A3) and (A4), the AR coefficient is found to be

$$C_{\text{AR}} = \frac{-(\int_0^\infty \mathcal{D}_e(E) \times \mathcal{R}_E^{\text{AR}} dE)}{(\int_0^\infty \mathcal{D}_e(E) \times \exp(-(E - \mu_H)/k_B T_H) dE)^3} = \frac{2W d_e \sqrt{E_g}}{\sqrt{E_g/(k_B T_H)}} \times u\left(-\frac{1}{2}, -4, E_g/(k_B T_H)\right), \quad (\text{A8})$$

where $u(-\frac{1}{2}, -4, x)$ is the confluent hypergeometric function of the second kind,

$$u\left(-\frac{1}{2}, -4, x\right) = \frac{16}{105} \frac{1}{\sqrt{\pi}} \int_0^\infty z^{7/2} \sqrt{z+x} e^{-z} dz. \quad (\text{A9})$$

If we eliminate W from Eq. (A3) by using Eq. (A8), we obtain the analytic expression of $\mathcal{R}_E^{\text{II-AR}}$ as a function of μ_H , T_H , and C_{AR} , which was used for the simulation in Sec. III B.

Inclusion of the II and AR rate to the rate Eq. (1), modifies the steady-state solution for n_E as follows. Since the term $\mathcal{R}_E^{\text{II-AR}}$ works as a source term for carrier generation which does not contain n_E explicitly, we can treat it in parallel with $\mathcal{R}_E^{\text{sun}}$. In other words, we can regard that Eq. (1) is modified by a replacement: $\mathcal{R}_E^{\text{sun}} \rightarrow \mathcal{R}_E^{\text{sun}} + \mathcal{R}_E^{\text{II-AR}}$. Therefore, we can use the exact solution, Eq. (7), just by changing g in Eq. (10) by

$$g = \mathcal{R}_E^{\text{sun}} + \mathcal{R}_E^{\text{II-AR}}(\mu_H, T_H, C_{\text{AR}}). \quad (\text{A10})$$

The linear stability analysis was also performed in the simulation in Sec. III B with including the term $\mathcal{R}_E^{\text{II-AR}}$ in the rate equation. It modifies the linearized equation of motion, Eq. (18), with additional terms

$$\left. \frac{d}{dt} \delta n_E \right|_{\text{II-AR}} = \frac{\partial \mathcal{R}_E^{\text{II-AR}}}{\partial \mu_H} \delta \mu_H + \frac{\partial \mathcal{R}_E^{\text{II-AR}}}{\partial T_H} \delta T_H, \quad (\text{A11})$$

where $\delta \mu_H$ and δT_H can be expressed by δn_E by Eq. (19) with Eqs. (21) and (22). As a result, the response function $\Lambda(E, E')$ in Eqs. (28) and (31) is modified by a replacement: $\Lambda(E, E') \rightarrow \Lambda(E, E') + \Lambda^{\text{II-AR}}(E, E')$, where

$$\Lambda^{\text{II-AR}}(E, E') = \frac{A_{22} \partial_{\mu_H} \mathcal{R}_E^{\text{II-AR}} - A_{21} \partial_{T_H} \mathcal{R}_E^{\text{II-AR}}}{\det \hat{A}} \mathcal{D}_e(E') + \frac{A_{11} \partial_{T_H} \mathcal{R}_E^{\text{II-AR}} - A_{12} \partial_{\mu_H} \mathcal{R}_E^{\text{II-AR}}}{\det \hat{A}} E' \mathcal{D}_e(E'). \quad (\text{A12})$$

Finally, we check the validity of the expressions, Eqs. (A3)–(A5), by checking a fundamental law of physics, i.e., total energy

conservation. Since the II and AR processes in this model originate from the Coulomb interaction, i.e., a mutual interaction between the hot carriers, the total energy that the hot carriers have must be conserved in a strict sense while the total number of the carriers changes by these processes. This can be checked by computing the total energy generated in a HCSC per unit time through these processes. We confirmed that the total energy conservations

$$\int_0^\infty \mathcal{D}_e(E)(E_g + 2E)\mathcal{R}_E^{\text{II}} dE = 0, \quad (\text{A13})$$

$$\int_0^\infty \mathcal{D}_e(E)(E_g + 2E)\mathcal{R}_E^{\text{AR}} dE = 0, \quad (\text{A14})$$

$$\int_0^\infty \mathcal{D}_e(E)(E_g + 2E)\mathcal{R}_E^{\text{II-AR}} dE = 0 \quad (\text{A15})$$

are exactly fulfilled by inserting Eqs. (A3)–(A5).

REFERENCES

- ¹R. T. Ross and A. J. Nozik, "Efficiency of hot-carrier solar energy converters," *J. Appl. Phys.* **53**, 3813–3818 (1982).
- ²W. Shockley and H. J. Queisser, "Detailed balance limit of efficiency of p-n junction solar cells," *J. Appl. Phys.* **32**, 510–519 (1961).
- ³H.-H. Fang, S. Adjokatse, S. Shao, J. Even, and M. A. Loi, "Long-lived hot-carrier light emission and large blue shift in formamidinium tin triiodide perovskites," *Nat. Commun.* **9**, 243 (2018).
- ⁴D.-T. Nguyen, L. Lombé, F. Gibelli, S. Boyer-Richard, A. Le Corre, O. Durand, and J.-F. Guillemoles, "Quantitative experimental assessment of hot carrier-enhanced solar cells at room temperature," *Nat. Energy* **3**, 236–242 (2018).
- ⁵Y. Takeda, A. Ichiki, Y. Kusano, N. Sugimoto, and T. Motohiro, "Resonant tunneling diodes as energy-selective contacts used in hot-carrier solar cells," *J. Appl. Phys.* **118**, 124510-1–124510-10 (2015).
- ⁶Y. Takeda, T. Motohiro, D. König, P. Aliberti, Y. Feng, S. Shrestha, and G. Conibeer, "Practical factors lowering conversion efficiency of hot carrier solar cells," *Appl. Phys. Exp.* **3**, 104301-1–104301-3 (2010).
- ⁷Y. Takeda, "Requisites for highly efficient hot-carrier solar cells," in *Quantum Dot Solar Cells*, edited by J. Wu and Z. M. Wang (Springer, New York, 2014).
- ⁸A. Le Bris and J.-F. Guillemoles, "Hot carrier solar cells: Achievable efficiency accounting for heat losses in the absorber and through contacts," *Appl. Phys. Lett.* **97**, 113506 (2010).
- ⁹P. Würfel, A. S. Brown, T. E. Humphrey, and M. A. Green, "Particle conservation in the hot-carrier solar cell," *Prog. Photovolt. Res. Appl.* **13**, 277–285 (2005).
- ¹⁰P. Aliberti, Y. Feng, Y. Takeda, S. K. Shrestha, M. A. Green, and G. Conibeer, "Investigation of theoretical efficiency limit of hot carriers solar cells with a bulk indium nitride absorber," *J. Appl. Phys.* **108**, 094507 (2010).
- ¹¹K. Kamide, T. Mochizuki, H. Akiyama, and H. Takato, "Nonequilibrium theory on the conversion efficiency limit of solar cells including thermalization and extraction of carriers," *Phys. Rev. Appl.* **10**, 044069 (2018).
- ¹²J. A. Kash, "Carrier-carrier scattering: An experimental comparison of bulk GaAs and GaAs/Al_xGa_{1-x}As quantum wells," *Phys. Rev. B* **48**, 18336(R) (1993).
- ¹³D. W. Snoke, "Density dependence of electron scattering at low density," *Phys. Rev. B* **50**, 11583 (1994).
- ¹⁴R. Österbacka, G. Juška, K. Arlauskas, A. J. Pal, K.-M. Källman, and H. Stubbs, "Electric field redistribution and electroluminescence response time in polymeric light-emitting diodes," *J. Appl. Phys.* **84**, 3359 (1998).
- ¹⁵T. Bryllert, M. Borgstrom, T. Sass, B. Gustafson, L. Landin, L.-E. Wernersson, W. Seifert, and L. Samuelson, "Designed emitter states in resonant tunneling through quantum dots," *Appl. Phys. Lett.* **80**, 2681 (2002).
- ¹⁶P. Y. Yu and M. Cardona, *Fundamentals of Semiconductors: Physics and Material Properties*, 3rd ed. (Springer, New York, 2005).
- ¹⁷W. H. Knox, C. Hirsimann, D. A. B. Miller, J. Shah, D. S. Chemla, and C. V. Shank, "Femtosecond excitation of nonthermal carrier populations in GaAs quantum wells," *Phys. Rev. Lett.* **56**, 1191 (1986).
- ¹⁸H. Haug and S. W. Koch, *Quantum Theory of the Optical and Electronic Properties of Semiconductors* (World Scientific, Singapore, 1990).
- ¹⁹X. C. V. Shank, R. L. Fork, R. F. Leheny, and J. Shah, "Dynamics of photoexcited GaAs band-edge absorption with subpicosecond resolution," *Phys. Rev. Lett.* **42**, 112 (1979).
- ²⁰R. F. Leheny, J. Shah, R. L. Fork, C. V. Shank, and A. Migus, "Dynamics of hot carrier cooling in photo-excited GaAs," *Solid State Commun.* **31**, 809 (1979).
- ²¹T. Suzuki and R. Shimano, "Cooling dynamics of photoexcited carriers in Si studied using optical pump and terahertz probe spectroscopy," *Phys. Rev. B* **83**, 085207-1–085207-8 (2011).
- ²²J. R. Goldman and J. A. Prybyla, "Ultrafast dynamics of laser-excited electron distributions in silicon," *Phys. Rev. Lett.* **72**, 1364–1367 (1994).
- ²³A. J. Sabbah and D. M. Riffe, "Femtosecond pump-probe reflectivity study of silicon carrier dynamics," *Phys. Rev. B* **66**, 165217-1–165217-11 (2002).
- ²⁴K. Kash, J. Shah, D. Block, A. C. Gossard, and W. Wiegmann, "Picosecond luminescence measurements of hot carrier relaxation in III-V semiconductors using sum frequency generation," *Physica B* **134**, 189 (1985).
- ²⁵A. J. Nozik, C. A. Parsons, D. J. Dunlavy, B. M. Keyes, and R. K. Ahrenkiel, "Dependence of hot carrier luminescence on barrier thickness in GaAs/AlGaAs superlattices and multiple quantum wells," *Solid State Commun.* **75**, 297 (1990).
- ²⁶D. J. Westland, J. F. Ryan, M. D. Scott, J. I. Davies, and J. R. Riffat, "Hot carrier energy loss rates in GaInAs/InP quantum wells," *Solid State Electron.* **31**, 431 (2008).
- ²⁷G. J. Conibeer, D. König, M. A. Green, and J. F. Guillemoles, "Slowing of carrier cooling in hot carrier solar cells," *Thin Solid Films* **516**, 6948 (2008).
- ²⁸Y. Rosenwaks, M. C. Hanna, D. H. Levi, D. M. Szymd, R. K. Ahrenkiel, and A. J. Nozik, "Hot-carrier cooling in GaAs: Quantum wells versus bulk," *Phys. Rev. B* **48**, 14675 (1993).
- ²⁹D. Watanabe, N. Kasamatsu, Y. Harada, and T. Kita, *Appl. Phys. Lett.* **105**, 171904 (2014).
- ³⁰M. Li, J. Fu, Q. Xu, and T. C. Sum, "Slow hot-carrier cooling in halide perovskites: Prospects for hot-carrier solar cells," *Adv. Mater.* **31**, 1802486 (2019).
- ³¹Y. Takeda, T. Ito, T. Motohiro, D. König, S. Shrestha, and G. Conibeer, "Hot carrier solar cells operating under practical conditions," *J. Appl. Phys.* **105**, 074905 (2009).
- ³²S. H. Strogatz, *Nonlinear Dynamics and Chaos: With Applications to Physics, Biology, Chemistry, and Engineering* (Addison-Wesley, Boston, MA, 1994).
- ³³T. Eram and P. L. Chapman, "Comparison of photovoltaic array maximum power point tracking techniques," *IEEE Trans. Energy Convers.* **22**, 439–449 (2007).
- ³⁴P. Würfel, "Solar energy conversion with hot electrons from impact ionisation," *Sol. Energy Mater. Sol. Cells* **46**, 43–52 (1997).
- ³⁵N. K. Dutta and J. Nelson, "The case for Auger recombination in In_{1-x}Ga_xAs_yP_{1-y}," *J. Appl. Phys.* **53**, 74 (1982).
- ³⁶E. Kioupakis, P. Rinke, K. T. Delaney, and C. G. Van de Walle, "Indirect Auger recombination as a cause of efficiency droop in nitride light-emitting diodes," *Appl. Phys. Lett.* **98**, 161107 (2011).
- ³⁷J. Piprek, *Semiconductor Optoelectronic Devices: Introduction to Physics and Simulation* (Academic Press, San Diego, 2003).
- ³⁸K. Seki, "Equivalent circuit representation of hysteresis in solar cells that considers interface charge accumulation: Potential cause of hysteresis in perovskite solar cells," *Appl. Phys. Lett.* **109**, 033905 (2016).
- ³⁹H. Haken, *Laser Light Dynamics*, Vol. 2 (North-Holland Physics Publishing, Amsterdam, 1985).
- ⁴⁰A. Luque and A. Martí, "Increasing the efficiency of ideal solar cells by photon induced transitions at intermediate levels," *Phys. Rev. Lett.* **78**, 5014–5017 (1997).
- ⁴¹K. Kamide, T. Mochizuki, H. Akiyama, and H. Takato, "Heat-recovery solar cell," *Phys. Rev. Appl.* **12**, 064001 (2019).